IEEE Access
Multidisciplinary ⋮ Rapid Review ⋮ Open Access Journal

Received August 2, 2020, accepted August 8, 2020, date of publication August 13, 2020, date of current version August 25, 2020.

Digital Object Identifier 10.1109/ACCESS.2020.3015975

Cirrus Detection Based on Tensor Multi-Mode Expansion Sum Nuclear Norm in Infrared Imagery

CHUNPING YANG, XUAN KONG, ZHAOYANG CAO, AND ZHENMING PENG, (Member, IEEE)
School of Information and Communication Engineering, University of Electronic Science and Technology of China, Chengdu 611731, China
Laboratory of Imaging Detection and Intelligent Perception, University of Electronic Science and Technology of China, Chengdu 610054, China

Corresponding author: Zhenming Peng (zmpeng@uestc.edu.cn)

This work was supported in part by the National Natural Science Foundation of China under Grant 61775030 and Grant 61571096; in part by the Open Research Fund of Key Laboratory of Optical Engineering, Chinese Academy of Sciences, under Grant 2017LBC003; in part by the Sichuan Science and Technology Program under Grant 2019YJ0167; and in part by the Aeronautical Science Foundation of China under Grant 2016018001.

ABSTRACT Infrared small target detection systems are an important part of space infrared imaging satellites. However, small infrared target detection is often affected by cirrus false alarm sources with similar grayscales. In this article, an infrared cirrus detection method based on the tensor robust principal component analysis model (TRPCA) is proposed. The method treats multiple bands of remote sensing data as tensors, but classical tensor nuclear norms cannot represent the tensor rank well; therefore, we use tensor multi-mode expansion sum nuclear norm (TMESNN) to approximate the tensor rank better. First, a set of Landsat-8 data is transformed into a tensor model, and a TRPCA model is constructed by TMESNN and the L_1 norm. Then, this model is solved by Ket augments and the alternating direction method of multipliers (ADMM). Finally, Mallat wavelet transform is used to supplement information and remove clutter, and the final detection result is obtained by adaptive threshold segmentation. Compared with other optimization-based methods, this method has better detection performance and accuracy.

INDEX TERMS Tensor multi-mode expansion sum nuclear norm, cirrus detection, ADMM, Ket augments, wavelet transform.

I. INTRODUCTION

Space infrared imaging satellites play an important role in ground monitoring, natural resource exploration and early warning systems, and are a necessary tool for ground surveillance, observation, and early warning and interception of missiles or aircraft [1]. However, in satellite infrared images, some high-radiation terrain or phenomena in the imaging band has the same gray level as the target, which may cause false alarms in remote sensing early warning system. These terrains or phenomena are called false alarm sources [2]. There is an important false alarm source called cirrus [3]. As shown in FIGURE 1, cirrus is marked with red boxes. It is usually weak, and its visual characteristic is similar to infrared military targets, which cause false alarms in remote sensing early warning systems, so the study of cirrus detection in satellite infrared images is necessary.

FIGURE 1. Schematic diagram of a cirrus infrared image.

A. RELATED WORK

Early cloud detection methods used physical properties, such as reflectance, brightness and temperature [4]–[9], to extract clouds from images. Scholars have proposed many methods for cloud detection of temporal infrared data using observation images of more than two scenes at the same location but at different times [10]–[13]. Many artificial intelligence

The associate editor coordinating the review of this manuscript and approving it for publication was Yongqiang Zhao.

methods have also been used for satellite infrared image target detection [14]–[19], but these methods are not suitable for cirrus detection in real scenes because they require a large quantity of image data [20].

Targets such as missiles or aircraft appear as small targets in satellite infrared images. Cirrus has similar visual characteristics with these small targets, so the infrared small targets detection method can be introduced into cirrus detection. The detection methods of infrared small targets mainly include methods based on filtering and visual features [21]–[27], methods based on background continuity [28], [29] and methods based on optimization.

Due to the improvement in optimization methods, the accuracy of infrared small target detection is constantly improving [30]–[38]. In optimization methods, principal component analysis (PCA) is a classic model [39], which reduces the dimensionality of high-dimensional data, removes sparse irrelevant information, and obtains the main information. From another perspective, we can also treat cirrus as the sparse component in infrared images and obtain it by PCA. However, the PCA method is susceptible to outliers. The emergence of RPCA [40] solved this problem. Its basic idea is that under certain constraints, matrix Y is approximately decomposed into two different matrices, S and L, after optimization, one sparse and one low-rank. This idea has been used in image processing [41]–[43]. In infrared images, the rank of the background is low, and the cirrus false alarm source is relatively sparse. Therefore, sparse components of the infrared image such as cirrus clouds, noise and clutter can be obtained by RPCA.

In traditional remote sensing image detection, the image is usually expanded into a two-dimensional matrix and studied using classic image processing methods, which lose the inherent structural information of multispectral images. Tensors, as a multidimensional extended form of matrices, have proven to be superior in processing multidimensional data. In recent years, some scholars have constructed third-order tensors of infrared images for small target detection. First, the objective function is constructed according to characteristics of the tensor's background and target. Then, the objective function is solved and the detection results are obtained [23], [30], [32], [44], confirming that the combination of a tensor model and robust principal component analysis model can achieve good results. Based on small sample remote sensing data, this article proposes a method based on small sample data [45], which uses visual features and sparse and low-rank decomposition to detect cirrus.

B. MOTIVATION

The backgrounds of infrared images are usually a low-rank matrix under certain conditions because the certain nonlocal autocorrelation is the characteristic of the background. In addition, the target area of infrared images is small, so it is regarded as a sparse matrix. The infrared target detection problem is naturally transferred to the matrix decomposition model by the above theory. Cirrus is sparse relative to the background, which has a lower rank. The infrared image of the cirrus consists of sparse cirrus elements and low-rank background elements, so the cirrus detection problem can also be transformed into a matrix decomposition problem.

Tensors, as high-dimensional extensions of matrices, can be directly used to process high-dimensional data such as color images, videos [46]–[48], and hyperspectral images [48]–[52] and is faster and more efficient. Based on the same extension concept, TRPCA was proposed, also known as high-order RPCA or tensor recovery [53]. Remote sensing data with multiple bands can be regarded as a tensor data composed of height, width, and spectrum, so the TRPCA model can be used for tensor decomposition.

Sum of Nuclear Norms (SNN) was applied to the TRPCA model by Huang *et al.* [54], but its low rankness cannot effectively solve the rank optimization problem. Lu *et al.* applied the Tensor Nuclear Norm (TNN) to the TRPCA model [55], but TNN cannot well-represent the low rank of high dimensions. Yang *et al.* applied the Tensor Multi-mode Expansion Sum Nuclear Norm (TMESNN) to the TRPCA model [56], showing its powerful ability to capture hidden associations between different tensor modes. In the real world, high-dimensional data are more vulnerable to the serious damage of sparse noise. A large number of experiments have proven that, compared with SNN and TNN, the method based on TMESNN has advantages in PSNR and SSIM values. It has been shown that the use of TMESNN in the TRPCA model can approximate the tensor rank better, and thus achieve good results in tensor decomposition of high-dimensional data.

After tensor decomposition of high-dimensional data, the sparse components detected in multiple bands are obtained. However, the components of these bands are not complete targets, and there is clutter interference. Therefore, we use the wavelet transform method to fuse the sparse components detected in different frequency bands. It can not only eliminate clutter, but also supplement information to avoid the inability to detect a complete cirrus cloud in a single band. Finally, cirrus cloud images can be obtained.

Based on the above motivations, this article proposes three innovative points:

1) First, TMESNN is a better representation of the tensor rank, so this article developed a TRPCA model based on TMESNN. Then, the problem of the infrared cirrus detection was transformed into a problem of solving the TRPCA model.
2) Second, the proposed TRPCA model is solved by an improved ADMM framework. In addition, this framework use KET augments to expand tensors with lower order so that they become tensors with lower order, which greatly reduces the algorithm complexity and computational time of the proposed method.
3) The Mallat wavelet transform method is used to fuse the sparse components detected in different bands. It can not only remove clutter but also supplement the information, avoiding a single band that cannot detect

the complete cirrus cloud. Eventually, a cirrus image can be obtained.

The structure of this article is as follows. Section 2 briefly covers some basic concepts about tensors and solutions. In section 3, The structure of the TRPCA model based on TMESNN is comprehensively described, and the improved ADMM solution framework of the proposed model is derived. In section 4, tests are carried out on the model in section 3 under different scenarios with various evaluation indexes, which verify its effectiveness. Section 5 introduces the discussion in this article. Section 6 concludes.

II. PRELIMINARIES

Before constructing the model, we need to briefly review some basic concepts and preliminary knowledge. In this article, $\mathcal{A}$ is used to represent the tensor, A is used to represent the matrix, $\overrightarrow{a}$ is used to represent the vector, and a is used to represent the scalar.

A. THE FUNDAMENTALS OF TENSORS

Before constructing the model, we need to briefly comb through some basic concepts and preliminary knowledge. In this article, $\mathcal{A}$ is used to represent the tensor, A is used to represent the matrix, $\overrightarrow{a}$ is used to represent the vector, and a is used to represent the scalar. Tensors are structures that describes higher-dimensional data. Tensors are higher-order extensions of scalars, vectors, and matrices, so we can also represent scalars, vectors, and matrices as lower-order tensors. $\mathcal{A} \in R^{N_1 \times N_2 \times N_3}$ is a third-order tensor whose (n_1, n_2, n_3) element is $\mathcal{A}_{n_1,n_2,n_3}$. The column fibers, row fibers, and tube fibers of $\mathcal{A}$ are $\mathcal{A}(:, n_2, n_3)$, $\mathcal{A}(n_1, :, n_3)$ and $\mathcal{A}(n_1, n_2, :)$.

Tensors can also be seen as a stack of different matrices, whose horizontal, side and front slices are represented by $\mathcal{A}(n_1, :, :)$, $\mathcal{A}(:, n_2, :)$, $\mathcal{A}(:, :, n_3)$ or $\mathcal{A}_{n_1,:,:}$, $\mathcal{A}_{:,n_2,:}$, $\mathcal{A}_{:,:,n_3}$.

In the tensor system, there are many definitions similar to those in matrix theory. These definitions are briefly explained below:

Definition 1 (Tensor Expansion Operation): Unlike a matrix consisting of only rows and columns, the order l tensor has l modes. Accordingly, we obtain a matrix in each mode. For a tensor, the mode-i unfolding operation is represented by the following operations:

$$\mathrm{A}_{(i)} = \mathrm{reshape}(\mathcal{A}) \in R^{Ni \times (N_1 \cdots N_{i-1} N_{i+1} \cdots N_l)} \tag{1}$$

The mode-(1,…, k) unfolding operation of the tensor is expressed as:

$$\mathrm{A}_{[i]} = reshape_{[i]}(\mathcal{A}, \prod_{k=1}^{i} N_k, \prod_{k=i+1}^{l} N_k) \in R^{\prod_{k=1}^{i} N_k \times \prod_{k=i+1}^{l} N_k} \tag{2}$$

where reshape(·) is the representation of a tensor expansion operator [42]. The corresponding tensor operation is: unreshape(reshape($\mathcal{A}$)) = $\mathcal{A}$.

Definition 2 (Circ Operation [1]): The third-order tensor performs the cyclic expansion operation and is expressed as circ(·):

$$\mathrm{circ}(\mathcal{A}) = \begin{bmatrix} \mathrm{A}^{(1)} & \mathrm{A}^{(N_3)} & \cdots & \mathrm{A}^{(2)} \\ \mathrm{A}^{(2)} & \mathrm{A}^{(1)} & \cdots & \mathrm{A}^{(3)} \\ \vdots & \vdots & \ddots & \vdots \\ \mathrm{A}^{(N_3)} & \mathrm{A}^{(N_3-1)} & \cdots & \mathrm{A}^{(1)} \end{bmatrix} \tag{3}$$

where $\mathrm{A}^{(i)}$ represents the front slice of the tensor.

Definition 3 (t-product): According to the tensor expansion formula, the t-product of third-order tensors $\mathcal{A} \in R^{N_1 \times N_2 \times N_3}$ and $\mathcal{B} \in R^{N_1 \times N_2 \times N_3}$ is the product of matrices in different forms:

$$\mathcal{C} = \mathcal{A} * \mathcal{B} = \mathrm{unreshape}(\mathrm{circ}(\mathcal{A}) \cdot \mathrm{reshape}(\mathcal{B})) \tag{4}$$

where $*$ represents the t -product between tensors.

Definition 4 (Conjugate Transpose): If we take the adjunct transpose of the front slice of the third-order tensor $\mathcal{A} \in R^{N_1 \times N_2 \times N_3}$, and the order of the slices is reversed from 2 to N_3, then I obtains the adjunct transpose tensor $\mathcal{A}^T \in R^{N_2 \times N_1 \times N_3}$.

Definition 5 (Orthogonal Tensor): If the tensor $\mathcal{P}$ is an orthogonal tensor, then it fits the following equation:

$$\mathcal{P} * \mathcal{P}^{\mathcal{T}} = \mathcal{P}^{\mathcal{T}} * \mathcal{P} = \mathcal{I} \tag{5}$$

Definition 6 (Diagonal Tensor): $\mathcal{A} \in R^{I_1 \times I_2 \times \cdots \times I_N}$ is a diagonal tensor when its elements are satisfied, $i_1 = i_2 = \cdots = i_N$, and $a_{i_1 i_2 \cdots i_N} \neq 0$, the other elements are all 0.

Definition 7 (Matrix Nuclear Norm): Given the matrix $\mathrm{Z} \in R^{N_1 \times N_2}$, its nuclear norm is:

$$\|\mathrm{Z}\|_* = \sum\nolimits_r \sigma_r(\mathrm{Z}) \tag{6}$$

where $\sigma_r(\mathrm{Z})$ $(r = 1, 2, \ldots, \min(N_1, N_2))$ represents the singular value of the matrix Z.

Definition 8 (SNN [58]): Given the third-order tensor $\mathcal{A} \in R^{N_1 \times N_2 \times N_3}$, its SNN is $\sum_{i=1}^{3} \alpha_i \left\|\mathrm{A}_{(i)}\right\|_*$, the constraint α_i satisfies: $\sum_{i=1}^{3} \alpha_i = 1$.

Definition 9 (TNN [59]:) Given the third-order tensor $\mathcal{A} \in R^{N_1 \times N_2 \times N_3}$, its TNN is: $\sum_{i=1}^{N_3} \alpha_i \left\|\mathrm{A}^{(i)}\right\|_*$, and the constraint α_i satisfies: $\sum_{i=1}^{N_3} \alpha_i = 1$.

B. SOME MATH PRELIMINARIES

Definition 10 (ADMM Framework [60]): ADMM is an efficient computational framework for solving 2-block distributed convex optimization problems:

$$\begin{aligned} &\arg\min_{x,z} g(x) + h(z) \\ &\text{s.t. } \mathrm{E}x + Fz = b \end{aligned} \tag{7}$$

where $x \in R^n$, $z \in R^m$, $E \in R^{p\times n}$, $F \in R^{p\times m}$, $b \in R^p$, $g : R^n \to R$, and $h : R^m \to R$. The augmented Lagrangian function of this convex optimization problem is:

$$L(x, z, y) = g(x) + h(z) + \langle y, Ex + Fz - b\rangle + \frac{\rho}{2}\|Ex + Fz - b\|_2^2 \quad (8)$$

where y is a Lagrangian multiplier, and ρ is a regular coefficient. The iterative steps of ADMM are:

$$\begin{cases} x^{k+1} = \arg\min_x g(x) + \left\langle y^k, Mx\right\rangle + \frac{\rho}{2}\left\|Ex + Fz^k - b\right\|_2^2 \\ z^{k+1} = \arg\min_z h(z) + \left\langle y^k, Nz\right\rangle + \frac{\rho}{2}\left\|Ex^{k+1} + Fz - b\right\|_2^2 \\ y^{k+1} = y^k + \tau\rho\left(Ex^{k+1} + Fz^{k+1} - b\right) \end{cases} \quad (9)$$

where τ represents the step size, and k represents the number of iteration steps.

Definition 11 (Ket Augmentation [61]): Ket augmentation is an enhancement method that can transform low-order tensors into high-order tensors. Under the tensor train decomposition, the Ket augmented tensor provides a clearer representation of the local data structure compared with the original tensor. If there is little correlation between the dimensions of the tensor, the augmented version of the tensortrain rank is lower. Therefore, Ket augments are an effective preprocessing step to minimize rank.

Given a tensor $\mathcal{A} \in R^{m\times n\times r}$, the processing steps of Ket augmentation include the following three steps:

1) Factorization: $m = m_1 \times m_2 \times \cdots \times m_s$, $n = n_1 \times n_2 \times \cdots \times n_s$, convert the size of $\mathcal{A}$ to $m_1 \times m_2 \times \cdots \times m_s \times n_1 \times n_2 \times \cdots \times n_s \times r$;
2) Change the order of the dimensions of $\mathcal{A}$, convert the size to $m_1 \times n_1 \times m_2 \times n_2 \times \cdots \times m_s \times n_s \times r$;
3) Turn $\mathcal{A}$ into an augmented result of size $m_1n_1 \times m_2n_2 \times \cdots \times m_sn_s \times r$.

III. PROPOSED METHOD

The background of infrared images obtained in military and space applications are usually the sky, clouds, sea surface, etc. [62], and due to atmospheric refraction, dispersion, optical defocus of equipment, etc., the obtained images usually have some blur [63]. According to the analysis of background characteristics, the background of such an infrared image usually has a certain nonlocal autocorrelation, which can generally be regarded as a low-rank continuous matrix. Accordingly, as the area occupied by the pixels belonging to the infrared target is small relative to the background, it can be regarded as a sparse matrix [64]. The infrared target detection problem is naturally transferred to the matrix factorization model by the above theory. In general, we can use the following model to describe the infrared image of small target:

$$\mathrm{D} = \mathrm{R} + \mathrm{S} \quad (10)$$

where D is the original infrared image, R and S represent different matrix components after decomposition, one is low-rank, the other is sparse. By solving the following convex optimization problems, the matrix decomposition can be realized:

$$\min \|\mathrm{R}\|_* + \lambda \|\mathrm{S}\|_1 \quad s.t.\ \mathrm{D} = \mathrm{R} + \mathrm{S} \quad (11)$$

From the perspective of tensor analysis, performing RPCA calculations on high-dimensional data can fully mine the hidden data structure information. To solve matrix decomposition problems, RPCA is extended to TRPCA. The TRPCA optimization model can be extended from the matrix RPCA model:

$$\min_{\mathcal{R},\mathcal{S}} rank(\mathcal{R}) + \lambda \|\mathcal{S}\|_0 \quad s.t.\ \mathcal{D} = \mathcal{R} + \mathcal{S} \quad (12)$$

where $\mathcal{R}$ and $\mathcal{S}$ represent different tensor components after decomposition, one is low-rank, the other is sparse. According to the basic knowledge of tensors, the tensors in this model, whose sparse terms are represented by the L_0 norm, and their low-rank terms are approximated by the rank of tensors. FIGURE 2 is a model diagram of TRPCA.

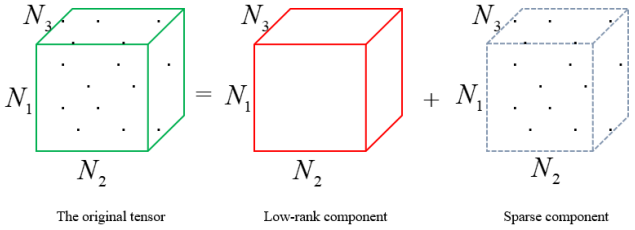

FIGURE 2. The model diagram of TRPCA.

Multiband remote sensing images can be regarded as third-order tensor data composed of multispectra, so the TRPCA model can be used for low-rank sparse decomposition.

A. TRPCA MODEL BASED ON TMESNN

Obviously, the TRPCA optimization model is an N-P hard problem. The L_1 norm of the tensor can be used to convex the L_0 norm of the tensor, but the representation of the tensor rank has always been a problem.

Some scholars use SNN to represent the tensor rank and apply it to TRPCA:

$$\min_{\mathcal{R},\mathcal{S}} \sum_{i=1}^{3} \alpha_i \left\|\mathrm{R}_{(i)}\right\|_* + \lambda \|\mathcal{S}\|_0 \quad s.t.\ \mathcal{D} = \mathcal{R} + \mathcal{S} \quad (13)$$

However, SNN cannot properly represent the global connection between different tensor models, because $\mathrm{A}_{(i)}$ represents the tensor expansion of a single model. When all models have the same dimension ($N_1 = N_2 = N_3 = N$), the size of $\mathrm{A}_{(i)}$ is $N \times N^2$, which cannot represent the connection of

high-dimensional data well. Later, some scholars proposed TNN and applied it to TRPCA:

$$\begin{aligned} &\min_{\mathcal{R},\mathcal{S}} \sum_{i=1}^{N_3} \alpha_i \left\| \mathcal{R}^{(i)} \right\|_* + \lambda \|\mathcal{S}\|_0 \\ &s.t.\ \mathcal{D} = \mathcal{R} + \mathcal{S} \end{aligned} \tag{14}$$

TNN is successfully applied to image restoration, and it has better results than SNN. However, in TNN, only one or two dimensions' connections are represented by t-SVD, which indicates that TNN lacks a low-rank representation of the third dimension and even higher dimensions.

Recently, TMESNN [61] was proposed:

$$\|\mathcal{R}\|_{\text{TMESNN}} = \sum_{i=1}^{l-1} \alpha_i \left\| \mathrm{R}_{[i]} \right\|_* \tag{15}$$

where the mode (1,..., k) expansion operation of tensor $\mathcal{R}$ is represented by $\mathrm{R}_{[i]} \in R^{\prod_{k=1}^{i} N_k \times \prod_{k=i+1}^{3} N_k}$, which is expanded by the first k modes and the last 3-k modes, and l is the tensor's dimension. TMESNN represents the relationship between different dimensions, which SNN and TNN cannot do. TMESNN is also used to solve mathematical problems: large-scale matrix singular value decomposition and so on.

This article uses the L_1 norm to the convex relax L_0 norm. Therefore, the cirrus detection model based on TRPCA is as follows:

$$\begin{aligned} &\min_{\mathcal{R},\mathcal{S}} \|\mathcal{R}\|_{\text{TMESNN}} + \lambda \|\mathcal{S}\|_1 \\ &s.t.\ \mathcal{D} = \mathcal{R} + \mathcal{S} \end{aligned} \tag{16}$$

where $\|\cdot\|_{\text{TMESNN}}$ represents TMESNN, and $\|\cdot\|_1$ represents the L_1 norms.

To solve ADMM in the next section, we convert (16) to the following problem by introducing auxiliary variables $\mathcal{V}_i$ $(i = 1, 2, \ldots, l-1)$ and $\mathcal{W}$:

$$\begin{aligned} &\min_{\mathcal{R},\mathcal{S}} \sum_{i=1}^{l-1} \alpha_i \|\mathcal{V}_i\|_* + \lambda \|W\|_1 \\ &s.t.\ \mathcal{V}_i = \mathrm{R}_{[i]}, \mathcal{D} = \mathcal{R} + \mathcal{S}, \mathcal{W} = \mathcal{S} \end{aligned} \tag{17}$$

B. SOLUTION OF THE PROPOSED MODEL

The expansion of the model is as follows:

The model constructed by TMESNN and the L_1 norm is solved by the ADMM framework. The augmented Lagrange function is:

$$\begin{aligned} &L(\mathcal{R}, \mathcal{S}, \mathcal{W}, \mathcal{V}_i, C_i, \varepsilon, \eta) \\ &= \sum_{i=1}^{l-1} \left(\alpha_i \|\mathcal{V}_i\|_* + \left\langle C_i, \mathcal{V}_i - R_{[i]} \right\rangle + \frac{\beta_i}{2} \left\| \mathcal{V}_i - R_{[i]} \right\|_F^2 \right) \\ &\quad + \lambda \|\mathcal{W}\|_1 \\ &\quad + \langle \eta, \mathcal{W} - \mathcal{S} \rangle + \frac{\sigma}{2} \|\mathcal{W} - \mathcal{S}\|_F^2 + \langle \varepsilon, \mathcal{D} - \mathcal{R} - \mathcal{S} \rangle \\ &\quad + \frac{\gamma}{2} \|\mathcal{D} - \mathcal{R} - \mathcal{S}\|_F^2 \end{aligned} \tag{18}$$

where C_i, ε and η represent the Lagrangian multiplier, β_i, σ and γ represent the penalty factor.

Then, ADMM is solved by the following iterative steps:

$$\begin{cases} \left(\mathcal{S}^{k+1}, \mathcal{R}^{k+1}\right) = \arg\min_{R,S} L(\mathcal{S}, \mathcal{R}, \mathcal{V}_i^k, \mathcal{W}^k, C_i^k, \eta^k, \varepsilon^k), \\ \left(\mathcal{V}_i^{k+1}, \mathcal{W}^{k+1}\right) = \arg\min_{R,S} L(\mathcal{S}^{k+1}, \mathcal{R}^{k+1}, \mathcal{V}_i, \\ \qquad \mathcal{W}, C_i^k, \eta^k, \varepsilon^k), \\ C_i^{k+1} = C_i^k + \tau\beta_i(\mathcal{V}_i^{k+1} - R_{[i]}^{k+1}), \\ \varepsilon_i^{k+1} = \varepsilon_i^k + \tau\gamma(\mathcal{D}^{k+1} - \mathcal{S}^{k+1} - \mathcal{R}^{k+1}), \\ \eta_i^{k+1} = \eta_i^k + \tau\sigma(\mathcal{W}^{k+1} - \mathcal{S}^{k+1}) \end{cases} \tag{19}$$

Next, we present the specific solution steps for each subproblem:

Subproblem of $(\mathcal{R}, \mathcal{S})$:

$$\begin{aligned} &\left(\mathcal{S}^{k+1}, \mathcal{R}^{k+1}\right) \\ &= \arg\min_{\mathcal{R},\mathcal{S}} L(\mathcal{S}, \mathcal{R}, \mathcal{V}_i^k, \mathcal{W}^k, C_i^k, \varepsilon^k, \eta^k) \\ &= \arg\min_{\mathcal{R},\mathcal{S}} \sum_{i=1}^{l-1} \left(\left\langle C_i^k, \mathcal{V}_i^k - R_{[i]} \right\rangle + \frac{\beta_i}{2} \left\| \mathcal{V}_i - R_{[i]} \right\|_F^2 \right) \\ &\quad + \left\langle \eta^k, \mathcal{W}^k - \mathcal{S} \right\rangle + \frac{\sigma}{2} \left\| \mathcal{W}^k - \mathcal{S} \right\|_F^2 \\ &\quad + \left\langle \varepsilon^k, \mathcal{D} - \mathcal{R} - \mathcal{S} \right\rangle \mathcal{S} + \frac{\gamma}{2} \|\mathcal{D} - \mathcal{R} - \mathcal{S}\|_F^2 \\ &= \arg\min_{\mathcal{R},\mathcal{S}} \sum_{i=1}^{l-1} \frac{\beta_i}{2} \left\| \mathcal{V}_i^k - R_{[i]} + C_i^k/\beta_i \right\|_F^2 \\ &\quad + \frac{\sigma}{2} \left\| W^k - S + \eta^k/\beta_i \right\|_F^2 + \frac{\gamma}{2} \left\| \mathcal{D} - \mathcal{R} - \mathcal{S} + \varepsilon^k/\gamma \right\|_F^2 \end{aligned} \tag{20}$$

Use $F(\mathcal{R}, \mathcal{S})$ to represent the objective function in equation (20), and use optimization condition $\partial F/\partial \mathcal{R} = 0$ and $\partial F/\partial \mathcal{S} = 0$ to obtain:

$$\begin{cases} \left(\sum_{i=1}^{3} \beta_i + \gamma \right) \mathcal{R} + \gamma \mathcal{S} \\ \qquad = \sum_{i=1}^{l-1} \beta_i \left(\text{unreshape}_{[i]} \left(\mathcal{V}_i^k + C_i^k \right) \Big/ \beta_i \right) \\ +\gamma \left(\mathcal{D} + \varepsilon^k \Big/ \gamma \right) \\ \gamma\mathcal{R} + (\gamma + \sigma)\mathcal{S} = \gamma \left(\mathcal{D} + \varepsilon^k \Big/ \gamma \right) \\ \qquad +\sigma \left(\mathcal{W}^k + \eta^k \Big/ \sigma \right) \end{cases} \tag{21}$$

From formula (21), we can solve:

$$\begin{cases} \mathcal{R}^{k+1} = \left(\gamma N^k - (\gamma + \sigma) M^k \right) \\ \qquad \Big/ \left(\gamma^2 - \left(\sum_{i=1}^{3} \beta_i + \gamma \right) (\gamma + \sigma) \right) \\ \mathcal{S}^{k+1} = \left(\gamma M^k - \left(\sum_{i=1}^{3} \beta_i + \gamma \right) N^k \right) \\ \qquad \Big/ \left(\gamma^2 - \left(\sum_{i=1}^{3} \beta_i + \gamma \right) (\gamma + \sigma) \right) \end{cases} \tag{22}$$

Among them:

$$\begin{cases} M^k = \sum_{i=1}^{l-1} \beta_i (\text{unreshape}_{[i]}(\mathcal{V}_i^k + C_i^k/\beta_i) + \gamma(\mathcal{D} + \varepsilon^k/\gamma) \\ N^k = \gamma(\mathcal{D} + \varepsilon^k/\gamma) + \sigma(\mathcal{W}^k + \eta^k/\sigma) \end{cases} \tag{23}$$

Subproblem of $\mathcal{W}$:

$$\begin{aligned} \mathcal{W}^{k+1} &= \arg\min_{\mathcal{W}} \lambda \|\mathcal{W}\|_1 \\ &\quad + \left\langle \eta^k, \mathcal{W} - \mathcal{S}^{k+1} \right\rangle + \frac{\sigma}{2} \left\| \mathcal{W} - \mathcal{S}^{k+1} \right\|_F^2 \\ &= \arg\min_{\mathcal{W}} \lambda \|\mathcal{W}\|_1 + \frac{\sigma}{2} \left\| \mathcal{W} - \mathcal{S}^{k+1} + \eta^k/\sigma \right\|_F^2 \end{aligned} \tag{24}$$

Using a soft thresholding operator [65], the following solution can be obtained:

$$\mathcal{W}^{k+1} = \max\left(\left| \mathcal{S}^{k+1} - \eta^k/\sigma \right| - \frac{\lambda}{\sigma}, 0 \right) \circ \frac{\mathcal{S}^{k+1} - \eta^k/\sigma}{\left| \mathcal{S}^{k+1} - \eta^k/\sigma \right|} \tag{25}$$

where $\circ$ is the Hadamard product, and $0 \circ \frac{0}{0}$ is defined as 0.

Subproblem of $\mathcal{V}_i$:

$$\begin{aligned} &\mathcal{V}_i^{k+1} \\ &= \arg\min_{\mathcal{V}_i} \sum_{i=1}^{l-1} \alpha_i \|\mathcal{V}_i\|_* + \left\langle C_i^k, \mathcal{V}_i - R_{[i]}^{k+1} \right\rangle \\ &\quad + \frac{\beta_i}{2} \left\| \mathcal{V}_{ii} - R_{[i]}^{k+1} \right\|_F^2 \\ &= \arg\min_{\mathcal{V}_i} \sum_{i=1}^{l-1} \left(\alpha_i \|\mathcal{V}_i\|_* + \frac{\beta_i}{2} \left\| \mathcal{V}_{ii} - R_{[i]}^{k+1} + C_i^k/\beta_i \right\|_F^2 \right) \end{aligned} \tag{26}$$

The subproblem of $\mathcal{V}_i$ can be split into $l-1$ subproblems:

$$\arg\min_{\mathcal{V}_i} \alpha_i \|\mathcal{V}_i\|_* + \frac{\beta_i}{2} \left\| \mathcal{V}_i - R_{[i]}^{k+1} + C_i^k/\beta_i \right\|_F^2 \quad (i = 1, 2, \ldots, l-1) \tag{27}$$

The solution to subproblem (27) is:

$$\mathcal{V}_i^{k+1} = V \Sigma_{\alpha_i/\beta_i} U^T \tag{28}$$

where $R_{[i]}^{k+1} - C_i^k/\beta_i = V\Sigma U^T$, $\Sigma_{\alpha_i/\beta_i} = \text{diag}\left(\max\left(\Sigma_{r,r} - \alpha_i/\beta_i\right), 0\right)$, and $\Sigma_{r,r}$ is an important component of Σ, which appears in this formula as the r-th singular value.

Algorithm 1 presents the whole algorithm:

Algorithm 1 Specific Steps of the ADMM Framework (17)

Input: The initial tensor $\mathcal{D}$, parameters λ, γ and σ.
Process:
Step 1: Initialize $\mathcal{R} = \mathcal{D}$, $\mathcal{V}_i$, $\mathcal{W}$, C_i, ε, η, maximum iteration step $K = 200$, $\tau = 1.1$.
Step 2: While $\left\|\mathcal{R}^{k+1} - \mathcal{R}^k\right\|_F / \left\|\mathcal{R}^k\right\|_F > \varepsilon$ and $k < K$ **Do**
Step 3: Update $\mathcal{R}$ and $\mathcal{S}$ by:

$$\begin{cases} \mathcal{R}^{k+1} = \left(\gamma N^k - (\gamma+\sigma) M^k\right) \Big/ \left(\gamma^2 - \left(\sum_{i=1}^{3} \beta_i + \gamma\right)(\gamma+\sigma)\right) \\ \mathcal{S}^{k+1} = \left(\gamma M^k - \left(\sum_{i=1}^{3} \beta_i + \gamma\right) N^k\right) \Big/ \left(\gamma^2 - \left(\sum_{i=1}^{3} \beta_i + \gamma\right)(\gamma+\sigma)\right) \end{cases}$$

Step 4: Update $\mathcal{W}$ by:

$$\mathcal{W}^{k+1} = \max\left(\left| \mathcal{S}^{k+1} - \eta^k \Big/ \sigma \right| - \frac{\lambda}{\sigma}, 0 \right) \circ \frac{\mathcal{S}^{k+1} - \eta^k/\sigma}{\left| \mathcal{S}^{k+1} - \eta^k/\sigma \right|}$$

Step 5: Update $\mathcal{V}_i$ by:

$$\mathcal{V}_i^{k+1} = V \Sigma_{\alpha_i/\beta_i} U^T$$

Step 6: Update C_i, ε and η by:

$$\begin{cases} C_i^{k+1} = C_i^k + \tau\beta_i(\mathcal{V}_i^{k+1} - R_{[i]}^{k+1}), \\ \varepsilon_i^{k+1} = \varepsilon_i^k + \tau\gamma(\mathcal{D}^{k+1} - \mathcal{R}^{k+1} - \mathcal{S}^{k+1}), \\ \eta_i^{k+1} = \eta_i^k + \tau\sigma(\mathcal{W}^{k+1} - \mathcal{S}^{k+1}) \end{cases}$$

Step 7: End Do
Output: Low-rank component $\mathcal{R}$ and sparse component $\mathcal{S}$.

C. BAND FUSION

Wavelet transform has many advantages such as accurate reconstruction, approximate human vision and multiresolution analysis, and has been widely used in image fusion [66]. The basic principle of band fusion based on wavelet transform is to decompose different bands, fuse the components of different frequencies, and finally, conduct inverse wavelet transform to obtain the final image. Selecting appropriate high-frequency fusion rules can preserve image edge features and remove clutter. The selection of low-frequency fusion rules determines the image's contour. The correct selection of fusion rules can improve the visual effect of fusion images.

The key steps of wavelet transform include decomposition, fusion and reconstruction, where reconstruction and decomposition are inverse processes to each other. The image is decomposed into different components of low and high frequency in three directions (horizontal, vertical, and diagonal) [1]. Wavelet decomposition is the principle of decomposition from coarse to fine, that is, from the first layer to the N-th layer.

Currently, the most widely used is the Mallat algorithm [68], which can improve the speed of image wavelet decomposition and reconstruction. Mallat uses two one-dimensional

filters to decompose two-dimensional images.

$$\begin{cases} C_j = H_c H_r C_{j-1} \\ D_j^H = G_c H_r C_{j-1} \\ D_j^V = H_c G_r C_{j-1} \\ D_j^D = G_c G_r C_{j-1} \end{cases} \tag{29}$$

where the low-frequency components of the layer j decomposition are represented by C_j, which is an approximation on C_{j-1}. D_j^H, D_j^V and D_j^D are high-frequency detail components of C_{j-1}. In the image, r is the row, c is the column, and j-1 is the number of decomposition layers. H represents low-pass filters. G represents the high-pass filters

Let the conjugate matrix of H and G be H^* and G^*. According to the Mallat reconstruction formulas, we can obtain:

$$C_{j-1} = H_r^* H_c^* C_j + H_r^* G_c^* C_j + G_r^* H_c^* C_j + G_r^* H_c^* C_j \tag{30}$$

According to the law of regional energy, the components of different frequencies are fused. The center of energy $E_J^i(x,y)$ is (x,y) and its region size is M × N:

$$E_J^i(x,y) = \sum_{x_0 \in M, y_0 \in N} \left[D_{K,J}^i (x + x_0, y + y_0) \right]^2 \tag{31}$$

where the decomposition coefficients of pixels in the K-th image at the J scale are represented by $D_{K,J}^i(x,y)$. Its fusion coefficient is:

$$F_J^i(x,y) = \begin{cases} D_{A,J}^i(x,y), E_{A,J}^i(x,y) \geq E_{B,J}^i(x,y) \\ D_{B,J}^i(x,y), E_{A,J}^i(x,y) < E_{B,J}^i(x,y) \end{cases} \tag{32}$$

where the wavelet coefficients $E_{A,J}^i(x,y)$ and $E_{B,J}^i(x,y)$ are derived from the source images A and B in the wavelet decomposition of the image layer j can be calculated by formula (31).

Assume the images of the band to be fused are $F_i (i = 1, 2, 3, \cdots, 7)$ and the fusion image is F. The specific steps are as follows:

1) An appropriate wavelet basis is selected to conduct N-layer discrete wavelet decomposition (DWT decomposition) of $F_i (i = 1, 2, 3, \cdots, 7)$. The end of each band can obtain one component with low frequency and 3N components with high frequencies:

$$\begin{cases} F = C_1^N + \sum_{j=1}^{N} \sum_{k=1}^{3} D_1^{j,k} \\ F_2 = C_2^N + \sum_{j=1}^{N} \sum_{k=1}^{3} D_2^{j,k} \\ \cdots \\ F_7 = C_7^N + \sum_{j=1}^{N} \sum_{k=1}^{3} D_7^{j,k} \end{cases} \tag{33}$$

where C_i^N represents the low-frequency component of F_i under the N-th decomposition layer, and $D_i^{j,k}$ is the high-frequency component of F_i in the three directions (horizontal, vertical and diagonal) under the N-th decomposition layer.

2) In each decomposition layer, fusion rule $f1$ and $f2$ are used to fuse the coefficients with different frequency. The fusion starts from the N-th layer and decreases successively until the 1st layer, that is, it can obtain one image F_c with low frequency and 3N images $F_D^{j,k}$ with high frequencies, where the conditions $j = 1, 2, 3, \cdots, N$, and $k = 1, 2, 3$ are satisfied. F_c and $F_D^{j,k}$ jointly constitute multiscale images.
3) To obtain the fused image, IDWT is performed on the multiscale image.

D. PROCESS SUMMARY OF THE PROPOSED METHOD

Algorithm 2 presents the general flow of the cirrus detection algorithm.

Algorithm 2 The General Flow of the Cirrus Detection Algorithm

Input: Infrared remote sensing image $Y \in R^{m \times n \times r}$, parameter λ, γ and σ.
Process:
Step 1: Take a part of the image Y for testing, the image size is 512 × 512, and the tensor with the size of 512 × 512 × 6 is formed
Step 2: Transform the 512 × 512 ×6 tensor into a 4 × 4 × 4 × 4 × 4 × 4 × 4 × 4 × 4 × 4 × 6 tensor using Ket augments,
Step 3: Construct the tensor robust principal component analysis model using TMESNN and the L_1 Norm
Step 4: Initialize $\mathcal{R} = \mathcal{D}, \mathcal{V}_i, \mathcal{W}, C_i, \varepsilon, \eta$,maximum iteration step $K = 200$, and $\tau = 1.1$. The TRPCA model is solved by the ADMM algorithm:
While $\|\mathcal{R}^{k+1} - \mathcal{R}^k\|_F / \|\mathcal{R}^k\|_F > \varepsilon$ and $k < K$ **Do**
Updating $\mathcal{R}$ and $\mathcal{S}$ by (22)
Updating $\mathcal{W}$ by (24)
Updating $\mathcal{V}_i$ by (38)
Updating C_i, ε and η by (19)
End Do
Step 5: Low-rank tensor $\mathcal{R}$ and sparse tensor $\mathcal{S}$ are used to reconstruct target image $F_i (i = 1, 2, 3, \cdots, 7)$ and background image $G_i (i = 1, 2, 3, \cdots, 7)$.
Step 6: Divide $F_i (i = 1, 2, 3, \cdots, 7)$ into N-layer discrete wavelet decomposition (DWT decomposition), and use the fusion rules to fuse the wavelet coefficients of each layer to obtain one image F_c with low frequency and 3N images $F_D^{j,k} (j = 1, 2, 3, \cdots, N, k = 1, 2, 3)$ with high frequencies, F_c and $F_D^{j,k}$ to form a multiscale image F'. Multiscale image F' is subjected to inverse discrete wavelet transform (IDWT) to obtain fused image F'
Step 7: Perform adaptive threshold segmentation on F' to obtain cirrus detection image C
Output: Cirrus detection image $C \in R^{m \times n}$

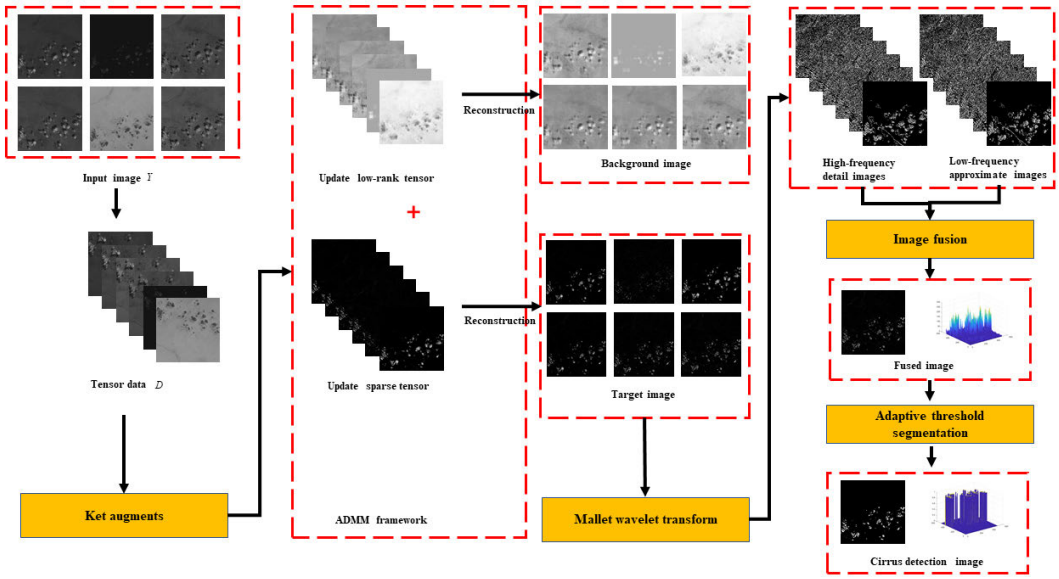

FIGURE 3. The overall flow chart of infrared cirrus detection method based on TMESNN.

The Landsat-8 data is used in the experiment in this article, and its satellite is a successor to the U.S. Landsat series [69]. Landsat-8 was launched on February 11, 2013, and is equipped with a thermal infrared sensor (TIRS) and the Operational Land Imager (OLI). The nine sensor bands of the OLI can cover the wavelength range from infrared to visible light. The TIRS includes 2 separate thermal infrared bands. The satellite captures data in 11 mutually registered spectral bands, which can be regarded as a tensor data composed of height, width and spectrum. Because the attributes of similar bands are basically coincident, six bands related to cloud attributes are selected.

FIGURE 3 visually describes the overall process of the infrared cirrus detection algorithm based on TMESNN. For this flowchart, the specific text description is also given:

1) Tensor Construction. Given a set of Landsat-8 data, using its 6 band images: Band 4 (the band range is 0.630–0.680μm), Band 5 (the band range is 0.845–0.885 μm), Band 6 (the band range is 1.560–1.660μm), Band 7 (the band range is 2.100–2.300μm), Band 9 (the band range is 1.360–1.390μm), Band 10 (the band range is 10.60 -11.19μm). Take a part of the image for testing, the image size is 512 $\times$ 512, and a tensor with the size of 512 $\times$ 512 $\times$ 6 is formed.
2) Separation of target and background. Using Ket augments, the 512 $\times$ 512 $\times$6 tensor is transformed into a 4 $\times$ 4 $\times$ 4 $\times$ 4 $\times$ 4 $\times$ 4 $\times$ 4 $\times$ 4 $\times$ 4 $\times$ 6 tensor. The input tensors are decomposed into low-rank tensors and sparse tensors by algorithm 2.
3) Image reconstruction and band fusion. Low-rank tensor and sparse tensor are used to reconstruct the target image and the background image. After that, the Mallet wavelet transform algorithm is used to fuse the target images of 6 bands, the wavelet basis function is the Morlet wavelet. Finally, the cirrus image is obtained by adaptive threshold segmentation.

IV. EXPERIMENT AND RESULTS

Nine groups of cirrus infrared images were tested in this article. The test data was from Landsat8 data with a resolution of 30 m. Each group of data includes 6 bands, and the specific meaning of each band is given in section 3. The original image was too large (7,621 $\times$ 7,751), and not every area had clouds, so a part of the image was taken for testing, the image size is 512 $\times$ 512, and 1.360–1.390 μm band image to show the cirrus distribution image. In FIGURE 4, (a) is from 37.82° $\sim$ 39.91° degrees east longitude and 105.65° $\sim$ 108.32° degrees south latitude. The shape of the cirrus is point-shaped and sparsely distributed throughout the image. (b) is from 46.92° $\sim$ 48.73° degrees east longitude and 78.15° $\sim$ 81.33° degrees south latitude, the cirrus is densely distributed in clusters, and the other areas are somewhat sparsely distributed. (c) is from 95.42° $\sim$ 98.63° degrees east longitude and 31.72° $\sim$ 33.76° degrees south latitude, the cirrus is distributed in clusters in the middle of the image. (d) is from 108.22° $\sim$ 111.63° degrees east longitude and 61.78° $\sim$ 64.13° degrees north latitude, there is only one cirrus and it is weak. (e) is from 95.15° $\sim$ 98.42° degrees east longitude and 72.09° $\sim$ 74.56° degrees north latitude, and the clustered cirrus is densely distributed. (f) is from 71.28° $\sim$ 74.67° degrees west longitude and 54.29° $\sim$ 56.36° degrees north latitude, and the cirrus is flocculent and densely distributed in the upper part of the water body. (g) is from 15.56° $\sim$ 17.67° degrees west longitude and 44.96° $\sim$ 47.35° degrees north latitude, and the cirrus clusters densely throughout the image. (h) is from 147.43° $\sim$ 149.87° degrees

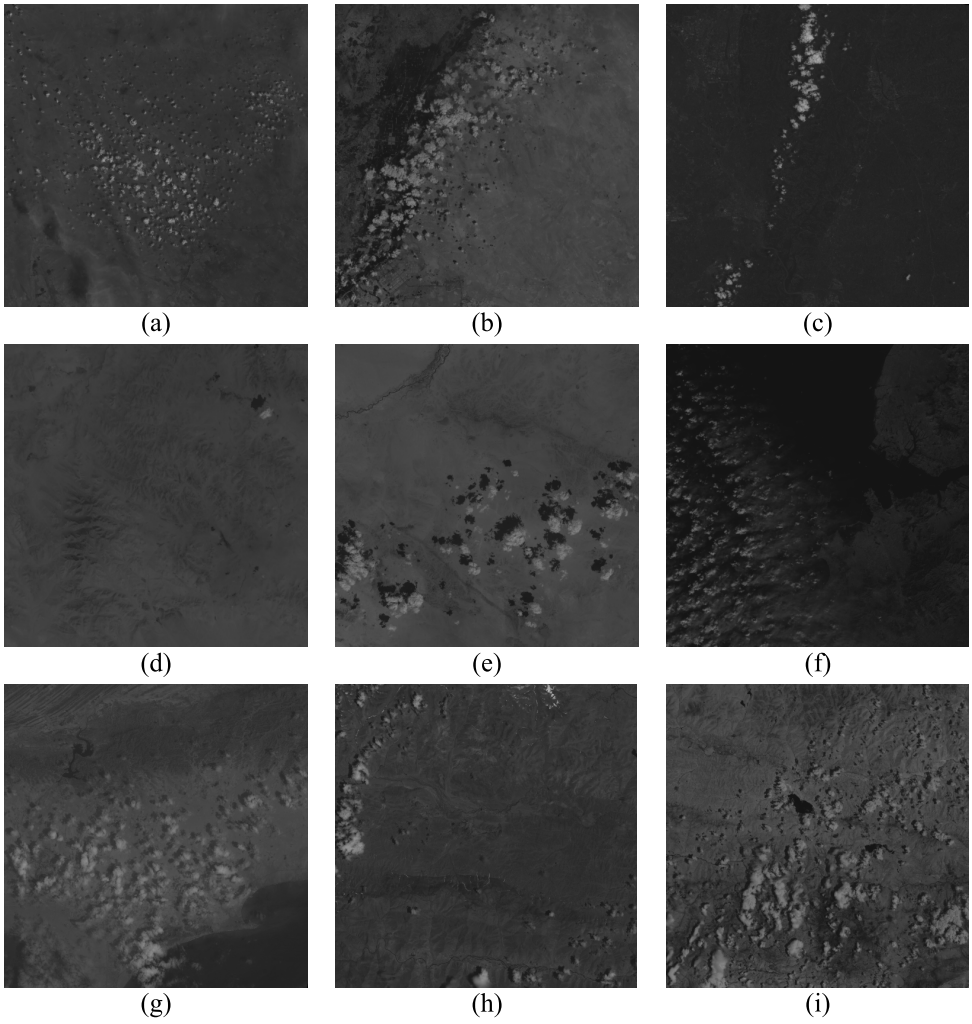

FIGURE 4. Images of cirrus in nine regions. (a)-(i) in the figure denote cirrus images of different regions and shapes.

FIGURE 5. Schematic diagram of the actual image and test image: (a) groundtruth image, (b) prediction image.

east longitude and 61.79° ∼ 63.45° degrees north latitude, and the cirrus is sparsely distributed in the whole image in the shape of dots. (i) is from 37.41° ∼ 39.63° degrees west longitude and 56.85° ∼ 58.90° degrees south latitude, the cirrus varies in size and is densely distributed throughout the image.

In this article, the cirrus detection method based on TMESNN is compared with other classical optimization methods, and its detection performance is evaluated qualitatively and quantitatively from several aspects. The experimental environment is an Intel Core i7-8550u 1.80 GHz CPU, Windows 10 OS with 8 GB memory, and MATLAB R2019a.

A. EVALUATION METRICS

During the detection, there are 4 cases: ① True Positive (TP), which predicts the target as the target, ② False Negative (FN), which detects the pixels in the background as the target, ③ True Negative (TN) means predicting the background as the background, ④ False Positive (FP) means predicting the target as the background. Since we are performing a supervised evaluation, we need to manually label the real cirrus mask image, which is shown in FIGURE 5(a). FIGURE 5(b) shows detected images. From these two figures, TP, FP, FN and TN are obtained.

The ROC curve is used to describe sensitivity. To obtain the ROC curve, we need to fit the relationship curve between the true positive rate (TPR) and false positive rate (FRR). The abscissa is the FPR and the ordinate is the TPR. The definitions of FPR and TPR are the following equations:

$$\mathrm{TPR} = \frac{TP}{TP + FN} \tag{34}$$

$$\mathrm{FPR} = \frac{FP}{TN + FP} \tag{35}$$

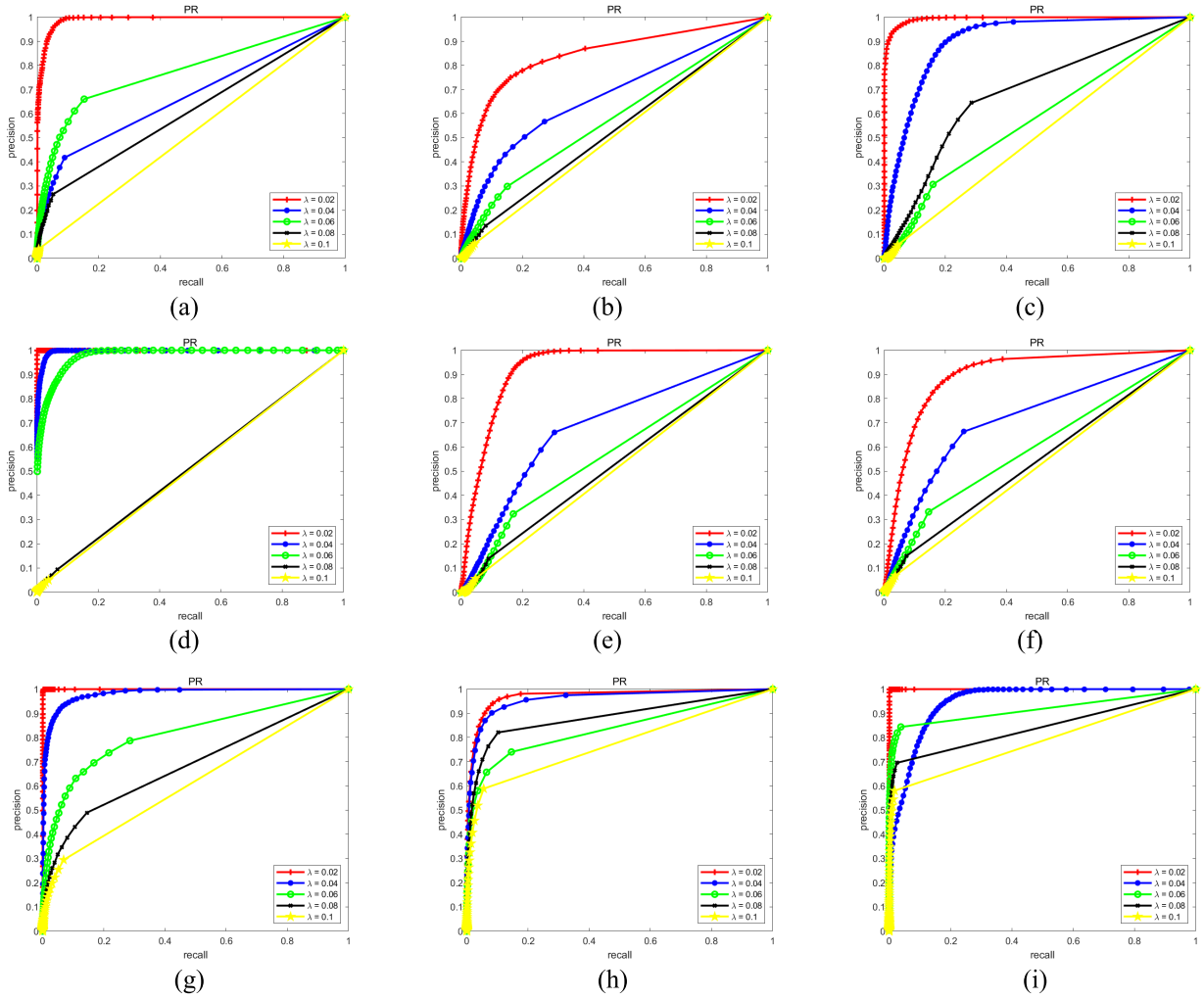

FIGURE 6. ROC curves of different λ values under nine scenes.

Generally, the larger the area under the curve (AUC) is, the better the method's detection effect represented by the ROC curve.

The PR curve is used to describe the performance of classification/retrieval. Its abscissa is recall and the ordinate is precision. The definitions of precision and recall are the following equations:

$$\text{precision} = \frac{TP}{TP + FP} \tag{36}$$

$$\text{recall} = \frac{TP}{TP + FN} \tag{37}$$

There may be a conflict between accuracy and recall, so a combination of the two is needed. The F-measure is the accuracy's weighted harmonic average:

$$\text{F-Measure} = \frac{\left(1 + \alpha^2\right) recall \times precision}{\alpha^2 \left(recall + precision\right)} \tag{38}$$

where α^2 is usually taken as 0.3, which will increase the weight of accuracy and that accuracy is more important than the recall rate.

The meaning of intersection-over-union (IOU) is to conduct threshold segmentation of the predicted image and calculate the ratio of intersection and union between it and the groundtruth image. The specific formula is as follows:

$$\text{IOU} = \frac{predicted \cap groundtruth}{predicted \cup groundtruth} \tag{39}$$

B. PARAMETER ANALYSIS

For the proposed model, several important parameters are taken as fixed values, for example, the iteration termination condition is set to $\left\|R^{k+1} - R^k\right\|_F / \left\|R^k\right\|_F \leq 10^{-4}$ and the weight is $\alpha_i = \frac{\delta_i}{\sum_{i=1}^{l-1} \delta_i}, \delta_i = \min\left(\prod_{k=1}^{i} n_k, \prod_{k=i+1}^{3} n_k,\right)$. However, some parameters, such as λ, γ, σ and β_i, usually affect the robustness of different scenarios. We use the ROC curve to qualitatively evaluate the local optimal values set by the parameters.

λ is a regularization parameter that can balance the proportional weight of sparse terms and low-rank terms, which is generally taken as $\lambda \in [0.01, 0.1]$, so we draw the ROC curve with $\lambda = [0.02, 0.04, 0.06, 0.08, 0.1]$, as shown

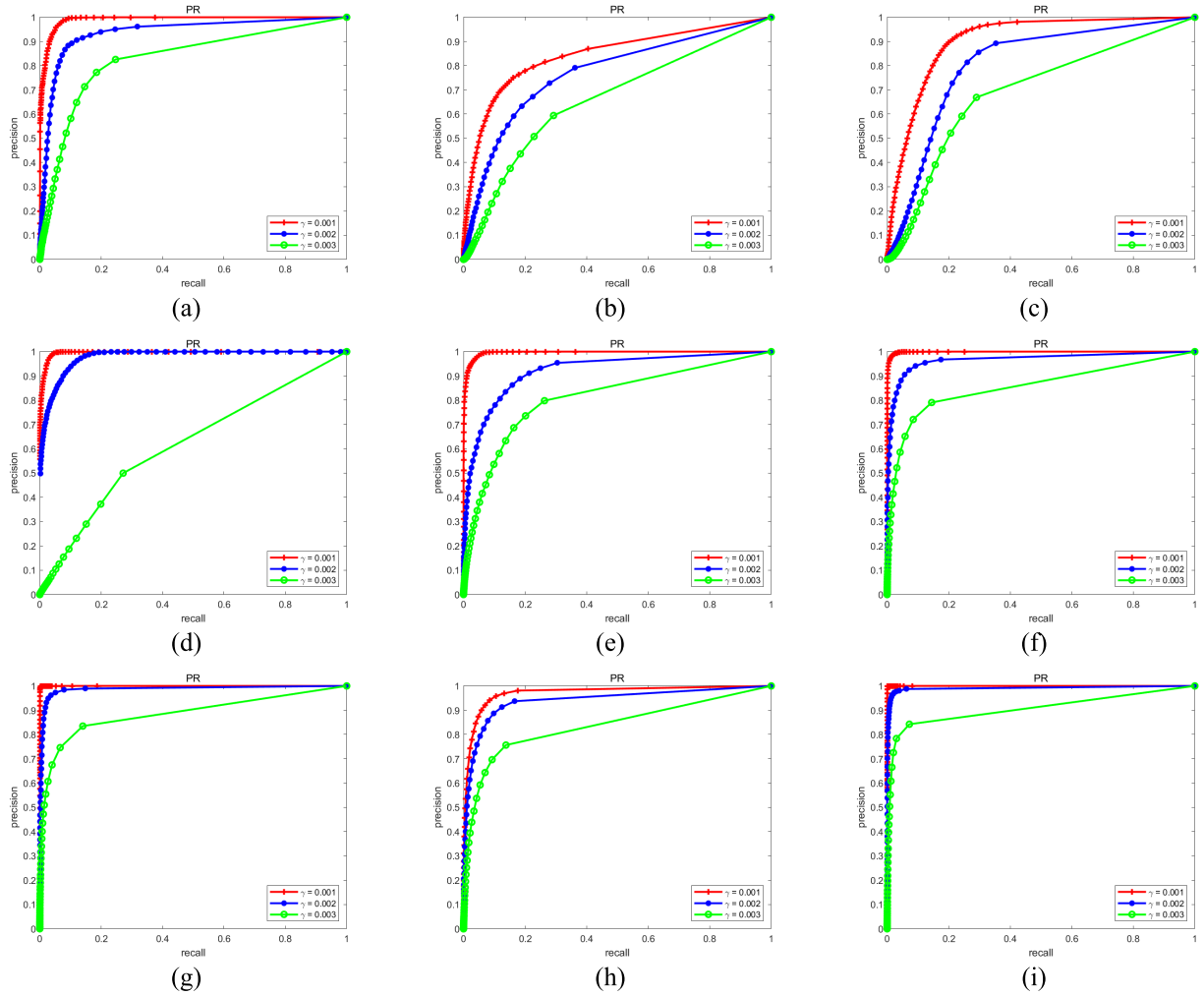

FIGURE 7. ROC curves of different γ values under nine scenes.

in FIGURE 6, and conclude that $\lambda = 0.02$ is the local optimal value.

γ is the penalty factor and is generally set as $\gamma \in [0.001, 0.003]$, so we draw the ROC curve with $\gamma = [0.001, 0.002, 0.003]$, as shown in FIGURE 7, and conclude that $\gamma = 0.001$ is the local optimal value.

The value range of σ is usually set as $[0.001, 0.01]$. Similar to the above steps of γ, we explore its five values $[0.001, 0.003, 0.005, 0.007, 0.009]$. In FIGURE 8, we can conclude that $\sigma = 0.001$ is the local optimal value by comparing the ROC curves.

β_i is the penalty factor, which satisfies $\beta_i = f\alpha_i$ and is generally $f \in \{0.1, 0.5, 1.1, 1.5\}$. Therefore, we draw the ROC curve with values in the set, as shown in FIGURE 9, and conclude that $f = 1.1$ is the local optimal value.

C. COMPARISON OF METHODS

The $512 \times 512 \times 6$ tensor is transformed into the $4 \times 4 \times 4 \times 4 \times 4 \times 4 \times 4 \times 4 \times 4 \times 6$ tensor, $l = 10$. The local optimal solution of each parameter is obtained through the above experiments, and the iteration termination condition needs to be set as: $\left\|R^{k+1} - R^k\right\|_F / \left\|R^k\right\|_F \leq 10^{-4}$, the weight is $\alpha_i = \delta_i / \sum_{i=1}^{3} \delta_i$, where $\delta_i = \min\left(\prod_{k=1}^{i} n_k, \prod_{k=i+1}^{3} n_k,\right)$, $(i = 1, 2, 3)$, regularization parameter $\lambda = 0.02$, penalty factor $\gamma = 0.001$, $\sigma = 0.001$ and $\beta_i = 1.1\alpha_i$. Then, the TMESNN-based cirrus detection method is applied to the test images of nine scenes.

In this article, the proposed method is compared with the PCA, RPCA, SNN and TNN methods; these methods all use wavelet transform and adaptive threshold segmentation. As shown in Figure 10, (a) is the original image. (b) is the cirrus detection image by the PCA method. (c) is the cirrus detection image by the RPCA method. (d) is the cirrus detection image by the SNN method. (e) is the cirrus detection image by the TNN method. (f) is the cirrus detection image by the proposed method. It is clear that the detection results by the proposed method are visually better than those by PCA, RPCA, SNN and TNN.

In this article, the ROC curve, PR curve, F-measure and IOU are used to qualitatively and quantitatively evaluate the

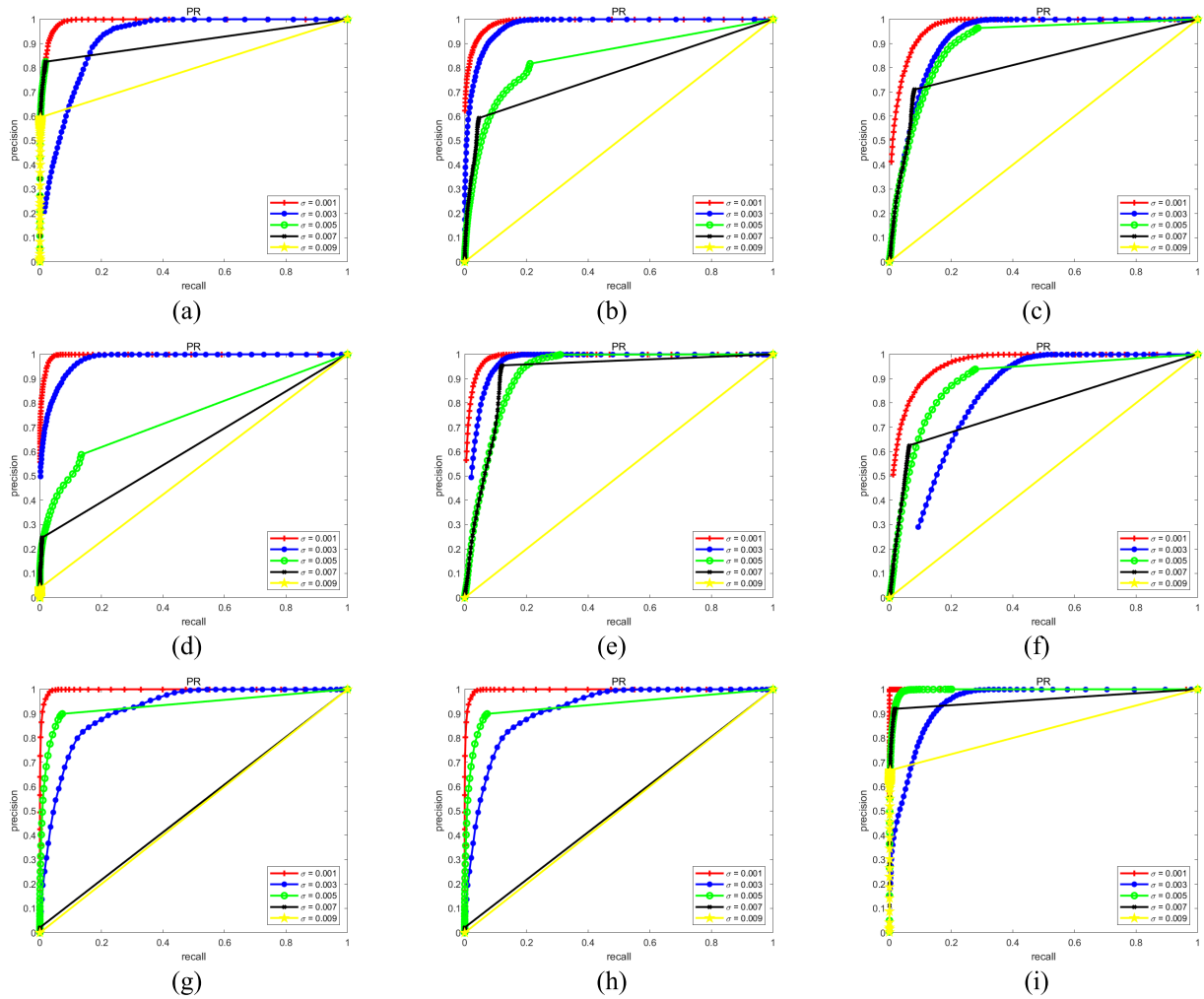

FIGURE 8. ROC curves of different σ values under nine scenes.

TABLE 1. AUC values of different ROC curves.

methods	PCA	RPCA	SNN	TNN	Proposed
test1	0.7188	0.9201	0.9426	0.7898	**0.9958**
test2	0.8211	0.7892	0.7209	0.8531	**0.9389**
test3	0.8335	0.8156	0.7174	0.9039	**0.9940**
test4	0.6554	0.6198	0.6150	0.9779	**0.9961**
test5	0.8648	0.7308	0.6370	0.9239	**0.9960**
test6	0.7032	0.9548	0.8924	0.8971	**0.9990**
test7	0.7319	0.9951	0.9783	0.9810	**0.9971**
test8	0.7878	0.9171	0.9176	0.9607	**0.9731**
test9	0.9613	0.9884	0.9881	0.9948	**0.9991**

proposed methods with the PCA, RPCA, SNN and TNN methods. As shown in FIGURE 11, the ROC curves of TMESNN and the PCA, RPCA, SNN and TNN methods were compared under nine scenarios. The figures in TABLE 1 are the AUC values of the ROC curves in FIGURE 11. If the value is closer to 1, the detection effect is better. The bold numbers represent the maximum values in several methods.

FIGURE 12 is a PR curve comparing TMESNN with the PCA, RPCA, SNN and TNN methods in nine scenarios. TABLE 2 shows the area under the PR curve in FIGURE 12.

TABLE 4 show the F-measures and IOU values for several methods respectively. These are the experimental results in nine different test scenarios. For each of the experiments in this article, to distinguish the maximum values in the table from the other values, they are shown in bold.

D. WAVELET TRANSFORM EXPERIMENT

In this article, Mallat wavelet transform is used to supplement information and remove clutter. To verify its effectiveness, we compare the method without wavelet transform

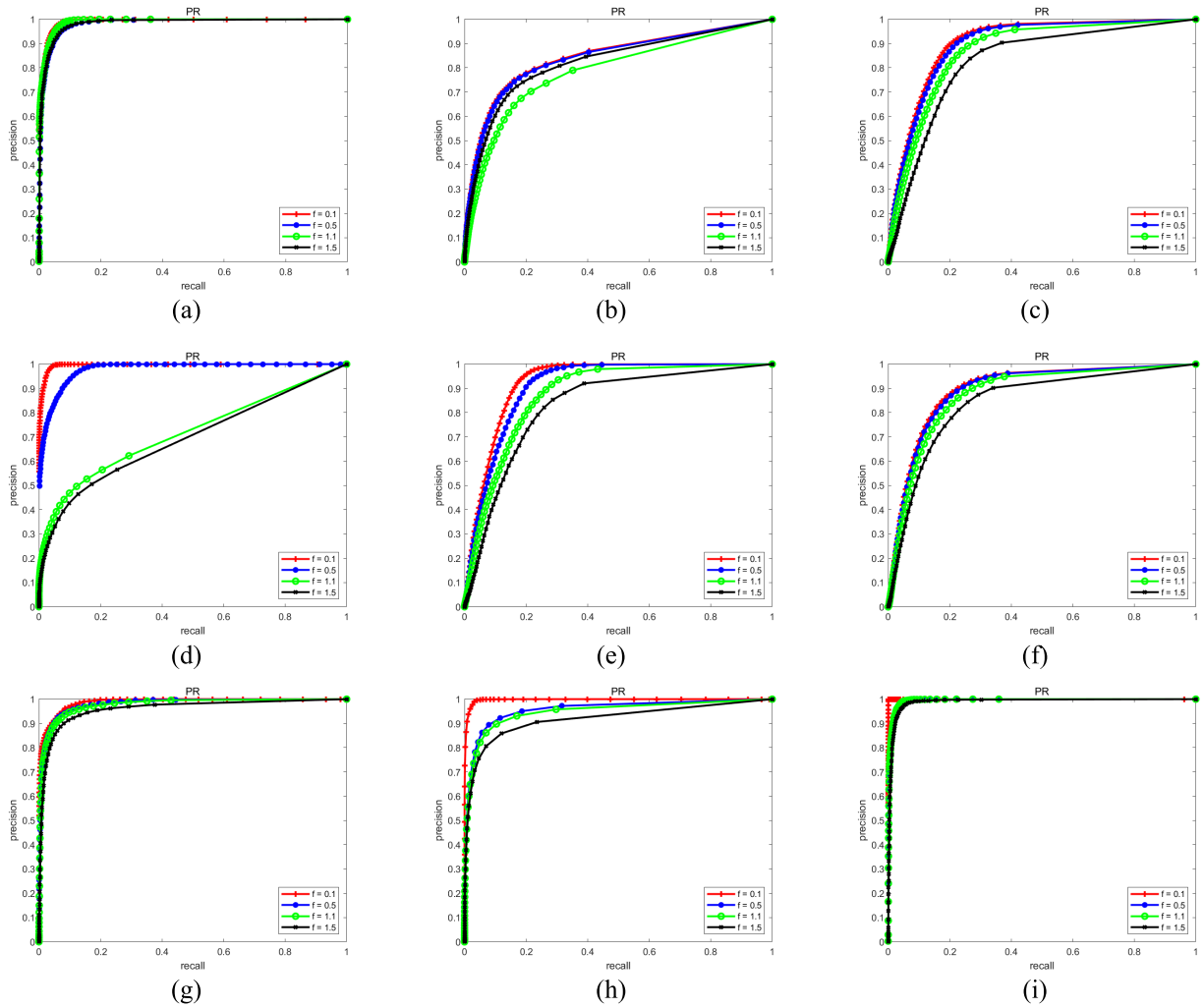

FIGURE 9. ROC curves of different f values under nine scenes.

TABLE 2. AUCpr values of different ROC curves.

methods	PCA	RPCA	SNN	TNN	Proposed
test1	0.0997	0.9420	0.9680	0.9680	**0.9980**
test2	0.2483	0.3072	0.1572	0.4035	**0.8451**
test3	0.2649	0.3155	0.1687	0.4364	**0.9604**
test4	0.3011	0.3104	0.2819	0.0914	**0.4254**
test5	0.1721	0.1547	0.0781	0.3121	**0.9496**
test6	0.1260	0.6532	0.3838	0.3644	**0.9893**
test7	0.0495	0.8174	0.5368	0.7019	**0.9978**
test8	0.2207	0.2958	0.3038	0.6776	**0.7252**
test9	0.3210	0.9745	0.9616	0.8012	**0.9981**

with methods using different wavelet basis functions; these functions include Haar, Mexihat and Morlet wavelets. Their wavelet decomposition and reconstruction methods are all the Mallat wavelet transform.

As shown in Figure 13, (a) is the original image. (b) is the cirrus detection image by the method without wavelet transform. (c) is the cirrus detection image by the method using the Haar wavelet basis function. (d) is the cirrus detection image by the method using the Mexihat wavelet basis function. (e) is the cirrus detection image by the method using the Morlet basis function. It is clear that the detection results by the method using the Morlet basis function are visually better than those by the other methods.

As shown in Figure 14, the ROC curves of the method without wavelet transform and the methods using different

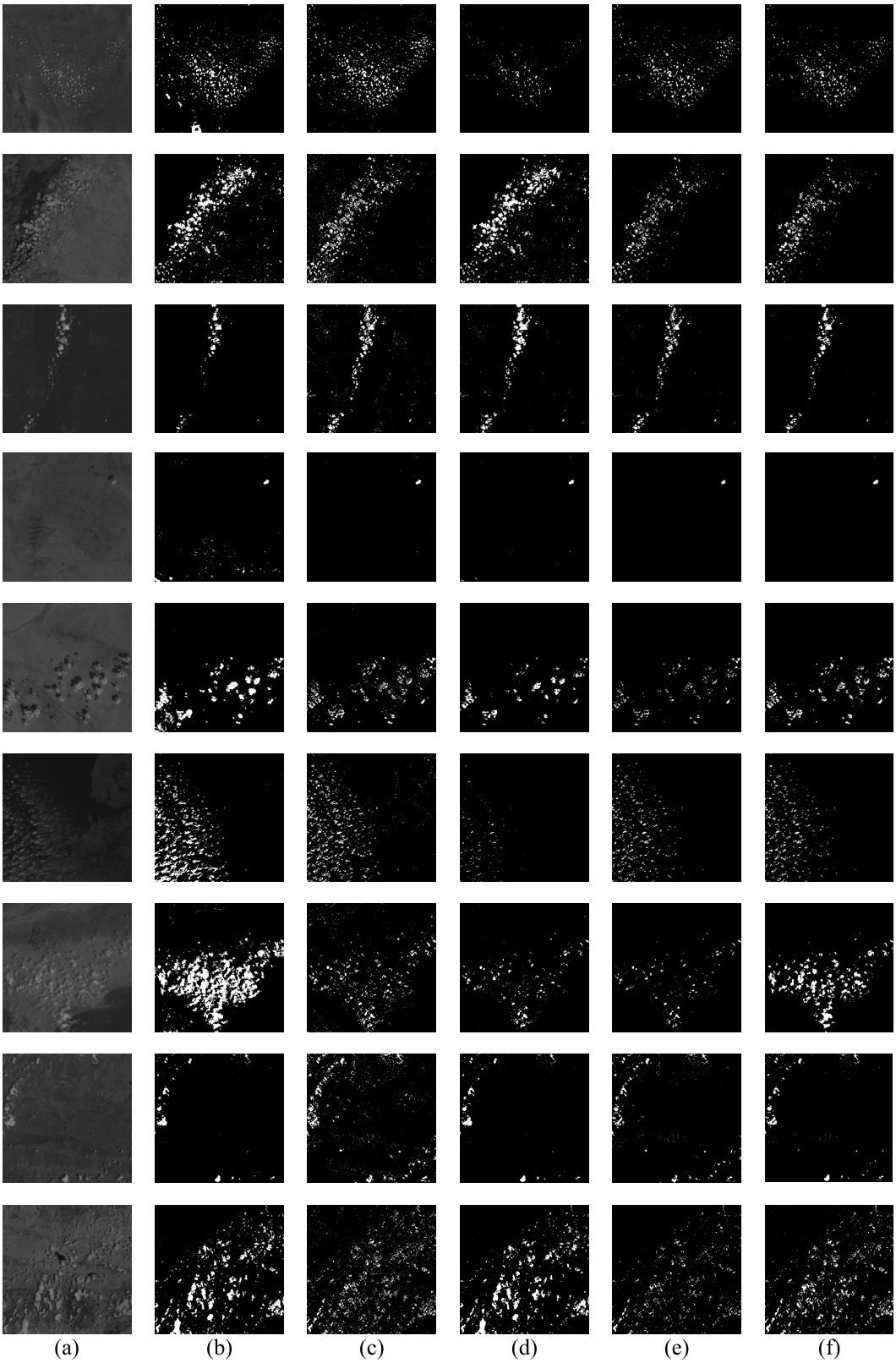

FIGURE 10. The experimental results of PCA, RPCA, SNN, TNN and the proposed method in test images of nine scenes: (a) is the original image, (b)-(f) are cirrus detection images by PCA, RPCA, SNN, TNN and the proposed method.

wavelet basis functions were compared under nine scenarios, ''no'' refers to ''the method without wavelet transform'', ''haar'', ''Mexihat'' and ''Morlet'' refer to methods using haar, Mexihat and Morlet wavelet basis functions The figures in TABLE 5 are the AUC values of the ROC curves in Figure 14. If the value is closer to 1, the detection effect

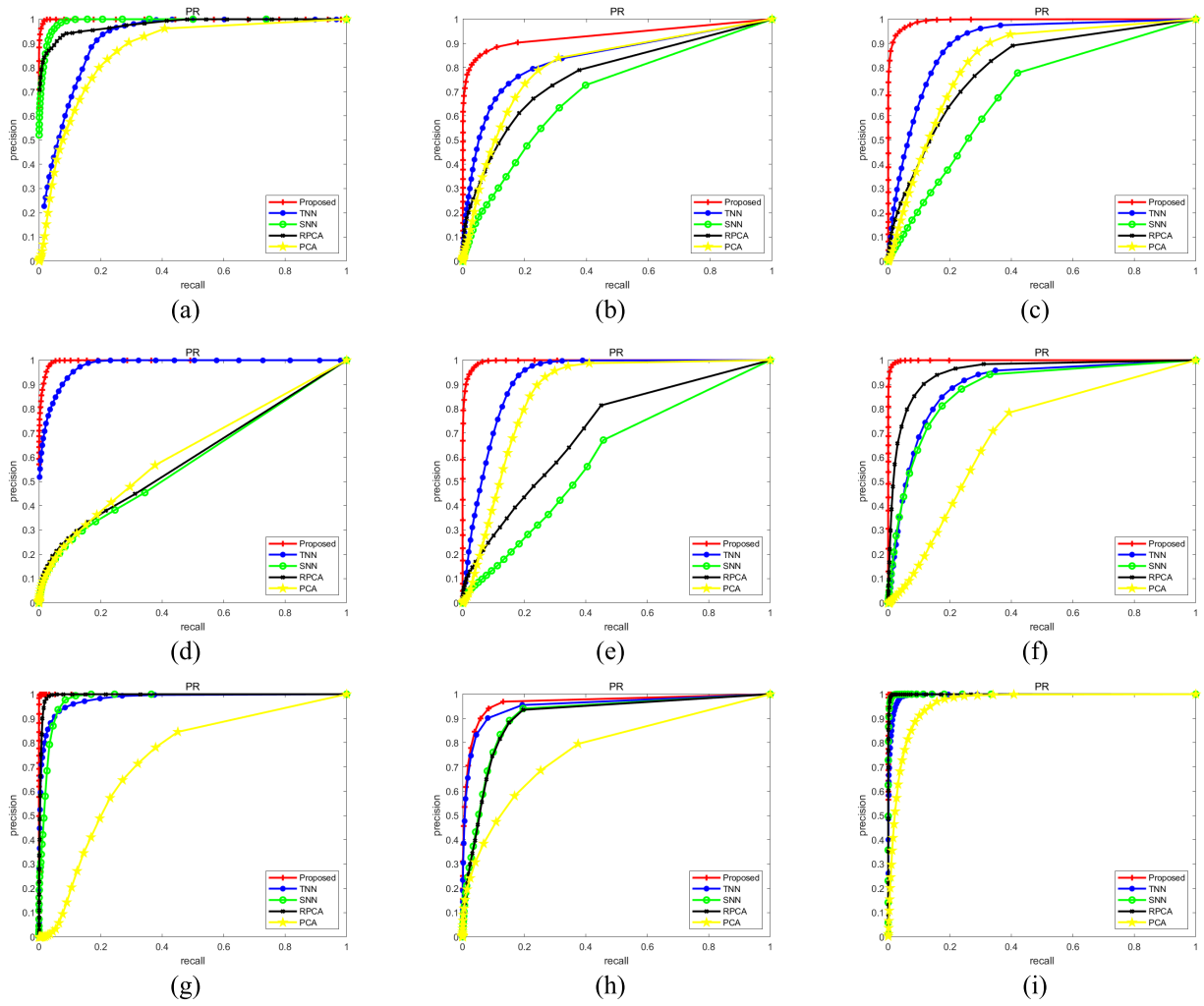

FIGURE 11. ROC curve of TMESNN compared with PCA, RPCA, SNN and TNN in nine scenarios.

TABLE 3. F-Measures corresponding to different methods in 9 scenes.

methods	PCA	RPCA	SNN	TNN	Proposed
test1	0.9159	0.9896	0.9861	0.9861	**0.9951**
test2	0.8990	0.9059	0.8856	0.9189	**0.9728**
test3	0.8507	0.8716	0.8409	0.8848	**0.9756**
test4	0.7976	0.8085	0.8022	0.8058	**0.8073**
test5	0.8741	0.8721	0.8575	0.8945	**0.9707**
test6	0.8450	0.9426	0.9092	0.9076	**0.9871**
test7	0.8082	0.8817	0.8712	0.8708	**0.8937**
test8	0.9526	0.9488	0.9487	0.9641	**0.9717**
test9	0.7271	0.8770	0.8700	0.8956	**0.9629**

is better. The bold numbers represent the maximum values in several methods.

E. ALGORITHM COMPLEXITY ANALYSIS

Real-time performance is the basic requirement of cirrus detection. However, it is difficult to reach a balance between the algorithm efficiency and its excellent accuracy, recall rate, IOU and F-measure. Traditional cirrus detection is often based on physical models, whose assumptions and calculations are simple and fast, but the accuracy is not ideal. A major drawback to optimization-based approaches is the complexity of the algorithm. Therefore, this section discusses the time complexity and computational time of different algorithms. Assuming that the size of the original remote sensing tensor data is $N_1 \times N_2 \times N_3$, for TRPCA based on TMESNN, the computational complexity of subproblem W

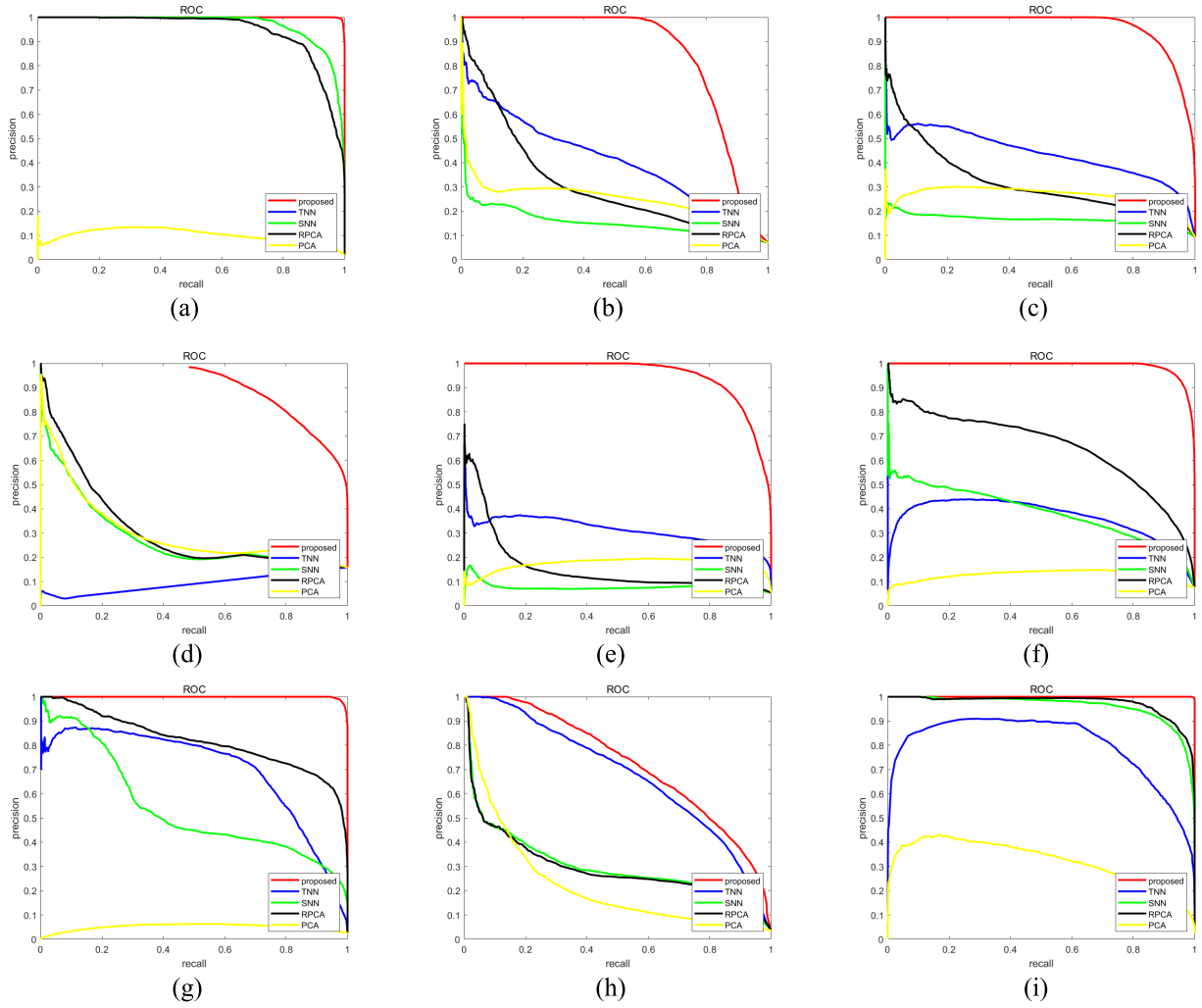

FIGURE 12. PR curve of TMESNN compared with PCA, RPCA, SNN and TNN in nine scenarios.

TABLE 4. IOU corresponding to different methods in 9 scenes.

methods	PCA	RPCA	SNN	TNN	Proposed
test1	0.6954	0.7658	0.7892	0.8442	**0.8764**
test2	0.7085	0.8238	0.7129	0.8178	**0.8590**
test3	0.6257	0.1949	0.1085	0.3323	**0.7743**
test4	0.7472	0.7367	0.8245	0.8053	**0.8408**
test5	0.6847	0.6996	0.7546	0.7089	**0.7563**
test6	0.5838	0.4236	0.6958	0.7036	**0.8492**
test7	0.5435	0.5476	0.3388	0.7635	**0.7981**
test8	0.6145	0.6819	0.6918	0.6514	**0.8929**
test9	0.7659	0.7511	0.6582	0.6839	**0.8333**

is $O\left(\prod_{i=1}^{l} N_i\right)$, the computational complexity of subproblem (R, S) is $O\left(\prod_{i=1}^{l} N_i\right)$, and the computational complexity of subproblem U_i is $O\left(\sum_{i=1}^{l-1} \min\left(p_i^2 q_i, p_i q_i^2\right)\right)$, where $\left(p_i = \prod_{k=1}^{i} n_k, q_i = \prod_{k=i+1}^{l} n_k\right)$. The total computational complexity is $O\left(\prod_{i=1}^{l} N_i + \sum_{i=1}^{l-1} \min\left(p_i^2 q_i, p_i q_i^2\right)\right)$.

Table 6 summarizes the algorithmic complexity of all the methods tested in this article and lists their average calculation time in 9 scenes of data in nine scenarios. We can see that the tensor-based optimization method takes longer than the low-level optimization method, but the TMESNN-based optimization method takes the least time among the tensor-based optimization methods.

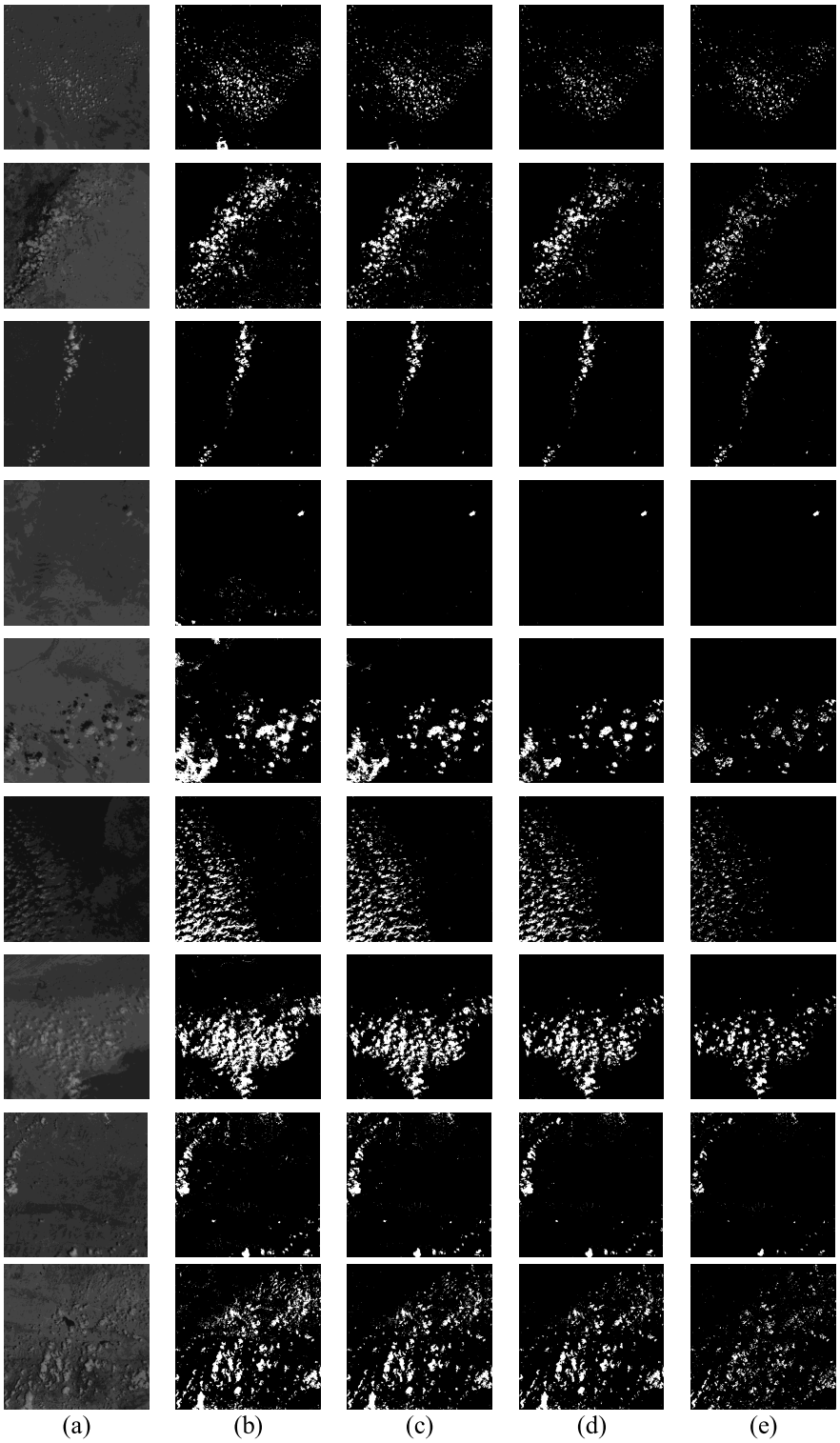

FIGURE 13. The experimental results of the method without wavelet transform and the methods using different wavelet basis functions in the test images of nine scenes: (a) is the original image, (b) are cirrus detection images by the method without wavelet transform, (c)-(e) are cirrus detection images by methods using different wavelet basis functions.

Experimental results verify the performance of the TMESNN-based TRPCA model. In FIGURE 11, the ROC curve of the model is close to the upper left corner, indicating that the detection performance is relatively good. In FIGURE 12, compared with other algorithms, the PR curve of the proposed algorithm is closer to the upper right corner,

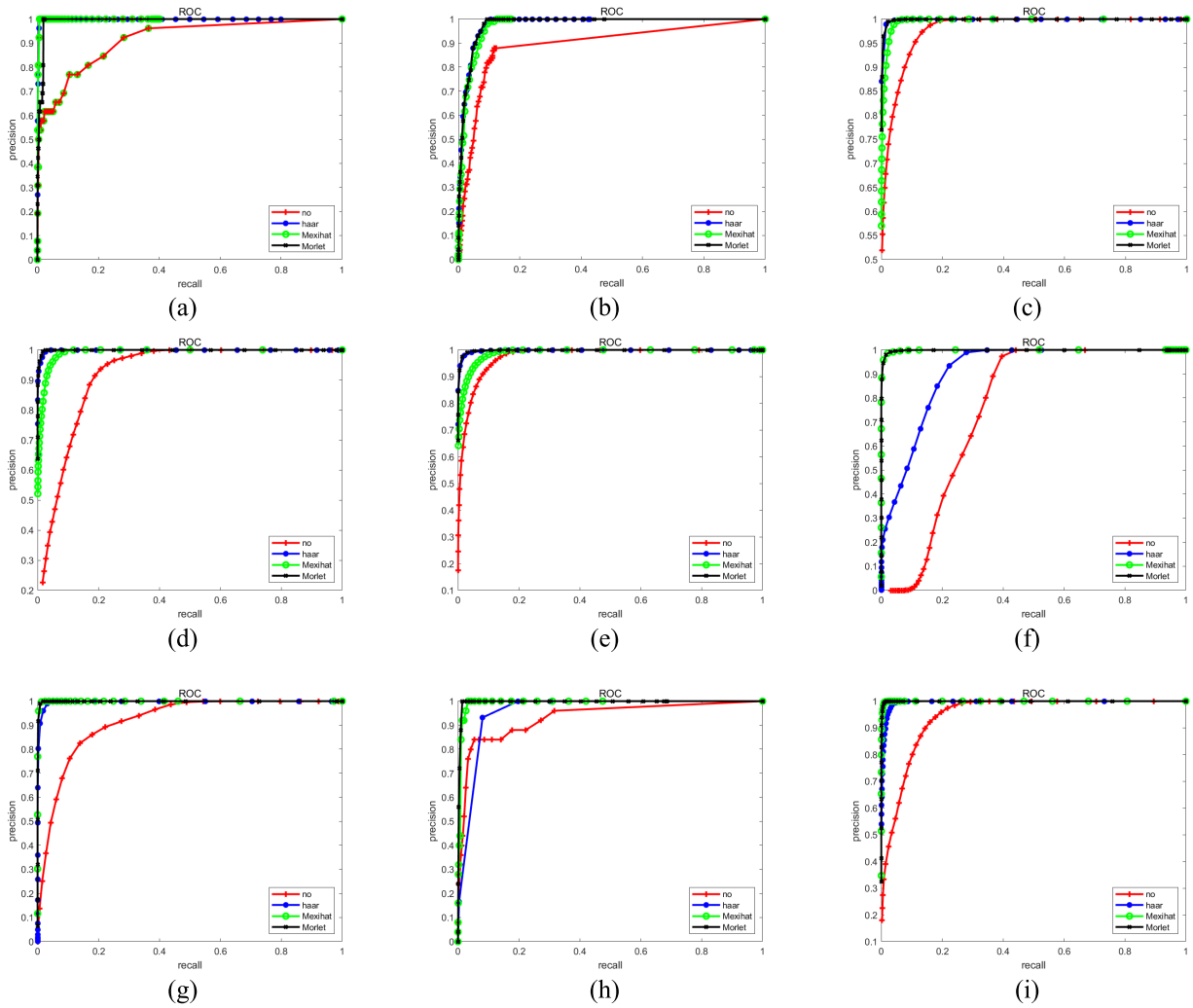

FIGURE 14. ROC curve of the method without wavelet transform and the methods using different wavelet basis functions in nine scenarios.

TABLE 5. AUC values of different ROC curves.

methods	no	haar	Mexihat	Morlet
test1	0.7926	0.9791	0.9747	**0.9958**
test2	0.8979	0.9247	0.9344	**0.9389**
test3	0.9165	0.9902	0.9913	**0.9940**
test4	0.8855	0.9889	0.9923	**0.9961**
test5	0.9465	0.9749	0.9758	**0.9960**
test6	0.7630	0.8948	0.9985	**0.9990**
test7	0.9107	0.9946	0.9952	**0.9956**
test8	0.9179	0.9280	0.9832	**0.9875**
test9	0.9022	0.9423	0.9902	**0.9911**

indicating a better detection effect. TABLE 1 and TABLE 2 show the AUC value and AUCpr value, respectively. The AUC value and AUCpr value of the proposed model are closer to 1, indicating that its detection effect is better, and the algorithm has a higher recall rate and a lower false alarm rate. TABLE 3 shows the F-measures of 9 scenarios. As seen from the values that are bold, the F-measure of this algorithm is higher than that of the other models.

TABLE 4 shows the IOU of 9 scenarios. The IOU value of this model is within the range of 0.7 to 0.9, which is higher than that of the other models and can directly indicate that the detection effect of this model is better. In FIGURE 14, compared with other methods, the ROC curve of the method using Morlet wavelet is closer to the upper right corner, indicating a better detection effect. In TABLE 5, the AUC value of the method using Morlet wavelet is closer to 1, indicating that its

TABLE 6. Complexity and computing time of various algorithms (in seconds).

Methods	Algorithm complexity	Time
PCA	$O\left(\left(N_1N_2\right)^3\right)$	3.655
RPCA	$O\left(N_1N_2^2\right)$	10.247
SNN	$O\left(N_1N_2N_3\left(N_1N_2+N_1N_3+N_2N_3\right)\right)$	71.785
TNN	$O\begin{pmatrix} N_1N_2N_3\log\left(N_3\right)+ \\ \max\left(N1,N2\right)\left(\min\left(N1,N2\right)\right)^2N_3 \end{pmatrix}$	52.268
Proposed	$O\left(\prod_{i=1}^{l}N_i+\sum_{i=1}^{l-1}\min\left(p_i^2q_i,p_iq_i^2\right)\right)$	39.064

detection effect is better. In this article TABLE 6 summarizes the algorithm complexity tests of different methods, and lists their average computational times in nine scenarios in the 9 groups of data; we can see that the optimization method based on tensor takes longer than the low-level optimization method, and the optimization method based on TMESNN based on tensor consumes the least time. In summary, the cirrus detection method virtual alarm source based on TMESNN has good infrared cirrus detection performance.

V. CONCLUSION

Aiming at the insufficient performance of cirrus detection methods based on physical attributes and its loss of multispectral data internal structural information, and the methods based on artificial intelligence relying on massive data, etc., an infrared image cirrus detection method based on tensor multimode expansion sum nuclear norm is proposed. This method makes full use of small sample data, which uses visual features and sparse and low-rank decomposition to detect cirrus.

This method regards multiple bands of remote sensing data as tensors, and combines the tensor multimode expansion sum nuclear norm and l1 norm to construct a tensor decomposition model, transforming the traditional cirrus detection task into a TRPCA problem, and TMESNN can represent the tensor rank better compared with existing tensor nuclear norms. This problem is solved by an efficient algorithm based on ADMM combined with Ket augmentation, which greatly reduces the algorithm complexity and calculation time and is faster than similar existing tensor-based methods. To remove clutter and supplementary information and avoid the problem that a single band cannot detect complete cirrus clouds, Mallat wavelet transform is used to fuse the sparse components of multiple bands. Finally, threshold detection is used to obtain cirrus cloud detection results. After many experiments, the ROC, PR, AUC, IOU value, F-Measures and other quality indicators show that this method has higher robustness in different environments than traditional optimization-based methods, and it is more robust with good detection performance and accuracy.

Although some progress has been made, there are still some shortcomings that need to be considered. For example, compared with optimization methods that do not contain tensors, this method has considerable room for improvement in real-time, so we need to explore more efficient methods. In addition, this method is suitable for small sample data and cannot use more advanced and efficient deep learning methods, so it is necessary to further expand the dataset.

ACKNOWLEDGMENT

The authors wish to thank the editors for their helpful suggestions.

REFERENCES

[1] L. Zunyang, Y. Qing, L. Xiuhe, S. Li, and S. Xiaoquan, "Choice and detectability of see-to-ground waveband of infrared warning satellite," *Infr. Laser Eng.*, vol. 47, no. 2, 2018, Art. no. 204003.

[2] Y. Wang, J. Huang, and X. Wei, "Infrared imaging simulation of space target in orbit," *Infr. Laser Eng.*, vol. 44, pp. 2593–2597, Sep. 2015.

[3] D. L. Mitchell, R. P. d'Entremont, and R. P. Lawson, "Inferring cirrus size distributions through satellite remote sensing and microphysical databases," *J. Atmos. Sci.*, vol. 67, no. 4, pp. 1106–1125, Apr. 2010.

[4] M. A. Lefsky, "Biomass accumulation rates of amazonian secondary forest and biomass of old-growth forests from Landsat time series and the geoscience laser altimeter system," *J. Appl. Remote Sens.*, vol. 3, no. 1, Dec. 2009, Art. no. 033505.

[5] S. Jin, C. Homer, L. Yang, G. Xian, J. Fry, P. Danielson, and P. A. Townsend, "Automated cloud and shadow detection and filling using two-date Landsat imagery in the USA," *Int. J. Remote Sens.*, vol. 34, no. 5, pp. 1540–1560, May 2013.

[6] Z. Zhu and C. E. Woodcock, "Object-based cloud and cloud shadow detection in Landsat imagery," *Remote Sens. Environ.*, vol. 118, pp. 83–94, Mar. 2012.

[7] Z. Zhu, S. Wang, and C. E. Woodcock, "Improvement and expansion of the Fmask algorithm: Cloud, cloud shadow, and snow detection for Landsats 4-7, 8, and Sentinel 2 images," *Remote Sens. Environ.*, vol. 159, pp. 269–288, Jan. 2015.

[8] L. Sun, J. Wei, J. Wang, X. Mi, Y. Guo, Y. Lv, Y. Yang, P. Gan, X. Zhou, C. Jia, and X. Tian, "A universal dynamic threshold cloud detection algorithm (UDTCDA) supported by a prior surface reflectance database," *J. Geophys. Res., Atmos.*, vol. 121, no. 12, pp. 7172–7196, Jun. 2016.

[9] H. Zhai, H. Zhang, L. Zhang, and P. Li, "Cloud/shadow detection based on spectral indices for multi/hyperspectral optical remote sensing imagery," *ISPRS J. Photogramm. Remote Sens.*, vol. 144, pp. 235–253, Oct. 2018.

[10] B. Wang, "Automated detection and removal of clouds and their shadows from Landsat TM images," *IEICE Trans. Inf. Syst.*, vol. 82, pp. 453–460, Jan. 1999.

[11] J. Chen, M. Lu, X. Chen, J. Chen, and L. Chen, "A spectral gradient difference based approach for land cover change detection," *ISPRS J. Photogramm. Remote Sens.*, vol. 85, pp. 1–12, Nov. 2013.

[12] S. Chen, X. Chen, and J. Chen, "An iterative haze optimized transformation for automatic cloud/haze detection of Landsat imagery," *IEEE Trans. Geosci. Remote Sens.*, vol. 54, no. 5, pp. 1–13, Jan. 2015.

[13] Z. Zhu and C. E. Woodcock, "Automated cloud, cloud shadow, and snow detection in multitemporal Landsat data: An algorithm designed specifically for monitoring land cover change," *Remote Sens. Environ.*, vol. 152, pp. 217–234, Sep. 2014.

[14] G. Cheng, P. Zhou, and J. Han, "Learning rotation-invariant convolutional neural networks for object detection in VHR optical remote sensing images," *IEEE Trans. Geosci. Remote Sens.*, vol. 54, no. 12, pp. 7405–7415, Dec. 2016.

[15] T. Bai, D. Li, and K. Sun, "Cloud detection for high-resolution satellite imagery using machine learning and multi-feature fusion," *Remote sensing.*, vol. 8, no. 9, pp. 1–21, Aug. 2016.

[16] F. Xie, M. Shi, Z. Shi, J. Yin, and D. Zhao, "Multilevel cloud detection in remote sensing images based on deep learning," *IEEE J. Sel. Topics Appl. Earth Observ. Remote Sens.*, vol. 10, no. 8, pp. 3631–3640, Aug. 2017.

[17] Z. Zhang, A. Iwasaki, and G. Xu, "Cloud detection on small satellites based on lightweight U-net and image compression," *J. Appl. Remote Sens.*, vol. 13, no. 2, pp. 457–468, Apr. 2019.

[18] J. Rabbi, N. Ray, M. Schubert, S. Chowdhury, and D. Chao, "Small-object detection in remote sensing images with end-to-end edge-enhanced GAN and object detector network," *Remote Sens.*, vol. 12, no. 9, p. 1423, May 2020.
[19] G. Zhang, S. Zhao, W. Li, Q. Du, Q. Ran, and R. Tao, "HTD-net: A deep convolutional neural network for target detection in hyperspectral imagery," *Remote Sens.*, vol. 12, no. 9, p. 1489, May 2020.
[20] M. Li, L. Peng, Y. Chen, S. Huang, F. Qin, and Z. Peng, "Mask sparse representation based on semantic features for thermal infrared target tracking," *Remote Sens.*, vol. 11, no. 17, p. 1967, Aug. 2019.
[21] Z. Peng, Q. Zhang, J. Wang, and Q. P. Zhang, "Dim target detection based on nonlinear multi-feature fusion by Karhunen-Loeve transform," *Opt. Eng.*, vol. 43, no. 12, pp. 2954–2958, Dec. 2004.
[22] W. Wang, C. Li, and J. Shi, "A robust infrared dim target detection method based on template filtering and saliency extraction," *Infr. Phys. Technol.*, vol. 73, pp. 19–28, Aug. 2015.
[23] Y. Dai and Y. Wu, "Reweighted infrared patch-tensor model with both non-local and local priors for single-frame small target detection," *IEEE J. Sel. Topics Appl. Earth Observ. Remote Sens.*, vol. 10, no. 8, pp. 3752–3767, May 2017.
[24] H. Zhang, L. Zhang, D. Yuan, and H. Chen, "Infrared small target detection based on local intensity and gradient properties," *Infr. Phys. Technol.*, vol. 89, pp. 88–96, Dec. 2017.
[25] S. Huang, Y. Liu, Y. He, T. Zhang, and Z. Peng, "Structure-adaptive clutter suppression for infrared small target detection: Chain-growth filtering," *Remote Sens.*, vol. 12, no. 47, pp. 1152–1179, Dec. 2019.
[26] X. Fan, Z. Xu, J. Zhang, Y. Huang, and Z. Peng, "Dim small targets detection based on self-adaptive caliber temporal-spatial filtering," *Infr. Phys. Technol.*, vol. 85, pp. 465–477, Sep. 2017.
[27] S. Huang, Z. Peng, Z. Wang, X. Wang, and M. Li, "Infrared small target detection by density peaks searching and maximum-gray region growing," *IEEE Geosci. Remote Sens. Lett.*, vol. 16, no. 12, pp. 1919–1923, May 2019.
[28] X. Fan, Z. Xu, J. Zhang, Y. Huang, and Z. Peng, "Infrared dim and small targets detection method based on local energy center of sequential image," *Math. Problems Eng.*, vol. 4572147, no. 1, pp. 1–16, Jul. 2017.
[29] X. Wang, Z. Peng, D. Kong, and Y. He, "Infrared dim and small target detection based on stable multisubspace learning in heterogeneous scene," *IEEE Trans. Geosci. Remote Sens.*, vol. 55, no. 10, pp. 5481–5493, Aug. 2017.
[30] H. Wang, F. Yang, C. Zhang, and M. Ren, "Infrared small target detection based on patch image model with local and global analysis," *Int. J. Image Graph.*, vol. 18, no. 1, Jan. 2018, Art. no. 1850002.
[31] L. Zhang, L. Peng, T. Zhang, S. Cao, and Z. Peng, "Infrared small target detection via non-convex rank approximation minimization joint $l_{2,1}$ norm," *Remote Sens.*, vol. 10, no. 11, p. 1821, Nov. 2018.
[32] L. Zhang and Z. Peng, "Infrared small target detection based on partial sum of the tensor nuclear norm," *Remote Sens.*, vol. 11, no. 4, p. 382, Feb. 2019.
[33] T. Zhang, H. Wu, Y. Liu, L. Peng, C. Yang, and Z. Peng, "Infrared small target detection based on non-convex optimization with Lp-norm constraint," *Remote Sens.*, vol. 11, no. 5, p. 559, Mar. 2019.
[34] X. Wang, Z. Peng, D. Kong, P. Zhang, and Y. He, "Infrared dim target detection based on total variation regularization and principal component pursuit," *Image Vis. Comput.*, vol. 63, pp. 1–9, Apr. 2017.
[35] X. Wang, Z. Peng, P. Zhang, and Y. He, "Infrared small target detection via nonnegativity-constrained variational mode decomposition," *IEEE Geosci. Remote Sens. Lett.*, vol. 14, no. 10, pp. 1700–1704, Aug. 2017.
[36] X. Fan, Z. Xu, J. Zhang, Y. Huang, Z. Peng, Z. Wei, and H. Guo, "Dim small target detection based on high-order cumulant of motion estimation," *Infr. Phys. Technol.*, vol. 99, pp. 86–101, Apr. 2019.
[37] L. Peng, T. Zhang, Y. Liu, M. Li, and Z. Peng, "Infrared dim target detection using Shearlet's kurtosis maximization under non-uniform background," *Symmetry*, vol. 11, no. 5, p. 723, May 2019.
[38] L. Peng, T. Zhang, S. Huang, T. Pu, Y. Liu, Y. Lv, Y. Zheng, and Z. Peng, "Infrared small-target detection based on multi-directional multi-scale high-boost response," *Opt. Rev.*, vol. 26, no. 6, pp. 568–582, Dec. 2019.
[39] S. Meng, L. T. Huang, and W. Q. Wang, "Tensor decomposition and PCA jointed algorithm for hyperspectral image denoising," *IEEE Geosci. Remote Sens. Letters.*, vol. 13, no. 7, pp. 1–5, Apr. 2016.
[40] E. J. Candès, X. Li, Y. Ma, and J. Wright, "Robust principal component analysis," *J. ACM*, vol. 58, no. 3, pp. 1–37, May 2011.
[41] T.-H. Oh, H. Kim, Y.-W. Tai, J.-C. Bazin, and I. S. Kweon, "Partial sum minimization of singular values in RPCA for low-level vision," in *Proc. IEEE Int. Conf. Comput. Vis.*, Dec. 2013, pp. 145–152.
[42] Z. Gao, L.-F. Cheong, and Y.-X. Wang, "Block-sparse RPCA for salient motion detection," *IEEE Trans. Pattern Anal. Mach. Intell.*, vol. 36, no. 10, pp. 1975–1987, Oct. 2014.
[43] Y. Lyu, L. Peng, T. Pu, C. Yang, J. Wang, and Z. Peng, "Cirrus detection based on RPCA and fractal dictionary learning in infrared imagery," *Remote Sens.*, vol. 12, no. 1, p. 142, Jan. 2020.
[44] X. Guan, L. Zhang, S. Huang, and Z. Peng, "Infrared small target detection via non-convex tensor rank surrogate joint local contrast energy," *Remote Sens.*, vol. 12, no. 9, p. 1520, Feb. 2020.
[45] X. Li, J. Wang, M. Li, Z. Peng, and X. Liu, "Investigating detectability of infrared radiation based on image evaluation for engine flame," *Entropy*, vol. 21, no. 10, p. 946, Sep. 2019.
[46] H. Yan, K. Paynabar, and J. Shi, "Image-based process monitoring using low-rank tensor decomposition," *IEEE Trans. Autom. Sci. Eng.*, vol. 12, no. 1, pp. 216–227, Jan. 2015.
[47] S. Hassanzadeh and A. Karami, "Compression and noise reduction of hyperspectral images using non-negative tensor decomposition and compressed sensing," *Eur. J. Remote Sens.*, vol. 49, no. 1, pp. 587–598, Sep. 2016.
[48] X. Gao, Y. Yang, D. Tao, and X. Li, "Discriminative optical flow tensor for video semantic analysis," *Comput. Vis. Image Understand.*, vol. 113, no. 3, pp. 372–383, Mar. 2009.
[49] X. Kong, Y. Zhao, J. Xue, and J. C.-W. Chan, "Hyperspectral image denoising using global weighted tensor norm minimum and nonlocal low-rank approximation," *Remote Sens.*, vol. 11, no. 19, p. 2281, Sep. 2019.
[50] X. Kong, Y. Zhao, J. Xue, J. C.-W. Chan, and S. G. Kong, "Global and local tensor sparse approximation models for hyperspectral image destriping," *Remote Sens.*, vol. 12, no. 4, p. 704, Feb. 2020.
[51] J. Xue, Y. Zhao, W. Liao, and J. Cheung-Wai Chan, "Nonconvex tensor rank minimization and its applications to tensor recovery," *Inf. Sci.*, vol. 503, pp. 109–128, Jul. 2019.
[52] J. Xue, Y. Zhao, W. Liao, and J. C.-W. Chan, "Nonlocal low-rank regularized tensor decomposition for hyperspectral image denoising," *IEEE Trans. Geosci. Remote Sens.*, vol. 57, no. 7, pp. 5174–5189, Mar. 2019.
[53] D. Goldfarb and Z. Qin, "Robust low-rank tensor recovery: Models and algorithms," *SIAM J. Matrix Anal. Appl.*, vol. 35, no. 1, pp. 225–253, Nov. 2014.
[54] B. Huang, C. Mu, and D. Goldfarb, "Provable models for robust low-rank tensor completion," *Pacific J. Optim.*, vol. 11, no. 2, pp. 339–364, Apr. 2015.
[55] C. Lu, J. Feng, Y. Chen, W. Liu, Z. Lin, and S. Yan, "Tensor robust principal component analysis: Exact recovery of corrupted low-rank tensors via convex optimization," in *Proc. IEEE Conf. Comput. Vis. Pattern Recognit.*, Jun. 2016, pp. 5249–5257.
[56] D. Bigoni, A. P. Engsig-Karup, and Y. M. Marzouk, "Spectral tensor-train decomposition," *SIAM J. Sci. Comput.*, vol. 38, no. 4, pp. A2405–A2439, Jan. 2016.
[57] M. E. Kilmer and C. D. Martin, "Factorization strategies for third-order tensors," *Linear Algebra Appl.*, vol. 435, no. 3, pp. 641–658, Aug. 2011.
[58] J. Liu, P. Musialski, P. Wonka, and J. Ye, "Tensor completion for estimating missing values in visual data," *IEEE Trans. Pattern Anal. Mach. Intell.*, vol. 35, no. 1, pp. 208–220, Jan. 2013.
[59] Z. Zhang, G. Ely, and S. Aeron, "Novel methods for multilinear data completion and de-noising based on tensor-SVD," in *Proc. IEEE Conf. Comput. Vis. Pattern Recognit.*, Jun. 2014, pp. 3842–3849.
[60] S. Boyd, "Distributed optimization and statistical learning via the alternating direction method of multipliers," *Found. Trends Mach. Learn.*, vol. 3, no. 1, pp. 1–122, Jan. 2010.
[61] J. A. Bengua, H. N. Phien, H. D. Tuan, and M. N. Do, "Efficient tensor completion for color image and video recovery: Low-rank tensor train," *IEEE Trans. Image Process.*, vol. 26, no. 5, pp. 2466–2479, Feb. 2017.
[62] X. Liu, Y. Chen, Z. Peng, J. Wu, and Z. Wang, "Infrared image super-resolution reconstruction based on quaternion fractional order total variation with lp quasinorm," *Appl. Sci.*, vol. 8, no. 10, p. 1864, Oct. 2018.
[63] X. Liu, Y. Chen, Z. Peng, and J. Wu, "Infrared image super-resolution reconstruction based on quaternion and high-order overlapping group sparse total variation," *Sensors*, vol. 19, no. 23, p. 5139, Nov. 2019.
[64] C. Gao, D. Meng, Y. Yang, Y. Wang, X. Zhou, and A. G. Hauptmann, "Infrared patch-image model for small target detection in a single image," *IEEE Trans. Image Process.*, vol. 22, no. 12, pp. 4996–5009, Dec. 2013.
[65] C. Wang, C. Li, and J. Wang, "A modified augmented Lagrange multiplier algorithm for toeplitz matrix completion," *Adv. Comput. Math.*, vol. 42, no. 5, pp. 1209–1224, Apr. 2016.

[66] X. Zhang, X. Li, and Y. Feng, "Image fusion based on simultaneous empirical wavelet transform," *Multimedia Tools Appl.*, vol. 76, no. 6, pp. 8175–8193, Mar. 2016.
[67] J. Li and L. Chang, "A SAR image compression algorithm based on mallat tower-type wavelet decomposition," *Optik Int. J. Light Electron Opt.*, vol. 126, no. 23, pp. 3982–3986, Aug. 2015.
[68] W. Habib, T. Sarwar, A. M. Siddiqui, and I. Touqir, "Wavelet denoising of multiframe optical coherence tomography data using similarity measures," *IET Image Process.*, vol. 11, no. 1, pp. 64–79, Nov. 2013.
[69] J. Zhao, J. Li, Q. Liu, W. Fan, B. Zhong, S. Wu, L. Yang, Y. Zeng, B. Xu, and G. Yin, "Leaf area index retrieval combining HJ1/CCD and Landsat8/OLI data in the Heihe river Basin, China," *Remote Sens.*, vol. 7, no. 6, pp. 6862–6885, May 2015.

CHUNPING YANG received the Ph.D. degree in optical engineering from the University of Electronic Science and Technology, in 2007. Since 1996, he has been engaged in scientific research and teaching with the Lidar Laboratory, University of Electronic Science and Technology. His main research interests include satellite-to-ground remote sensing system simulation and information processing, and infrared image processing and application.

XUAN KONG received the B.S. degree from the School of Physics, University of Electronic Science and Technology of China (UESTC), in 2019. He is currently pursuing the M.E. degree with the School of Information and Communication Engineering, UESTC. His research interests include image processing, signal and information processing, and infrared target detection.

ZHAOYANG CAO received the B.E. degree from the School of Optoelectronic Science and Engineering, University of Electronic Science and Technology of China (UESTC), in 2019. He is currently pursuing the M.E. degree with the School of Information and Communication Engineering, UESTC. His research interests include image processing, signal and information processing, and compressive sensing.

ZHENMING PENG (Member, IEEE) received the Ph.D. degree in geodetection and information technology from the Chengdu University of Technology, Chengdu, China, in 2001. From 2001 to 2003, he was a Postdoctoral Researcher with the Institute of Optics and Electronics, Chinese Academy of Sciences, Beijing, China. He is currently a Professor with the University of Electronic Science and Technology of China, Chengdu. His research interests include image processing, signal processing, and target recognition and tracking. He is a member of the China Optical Engineering Society (COES) and the Chinese Society of Astronautics (CSA).